Urban thermal and mechanical effects on surface warming and cold front structures over eastern China

Doctoral Thesis

博士論文

Urban thermal and mechanical effects on surface warming and cold front structures over eastern China

(中国東部における地表温度と寒冷前線構造に関する都市の熱的・力学的効果)

東北大学大学院理学研究科

地球物理学専攻

朱　心悦（Zhu Xinyue）

指導教員

佘　偉明　准教授

論文審査委員

山崎　剛　　准教授　(主査)

岩崎　俊樹　教授

早坂　忠裕　教授

須賀　利雄　教授

2014

平成 26 年

Abstract

Urban surface influences local weather and climate through thermal and mechanical effects. Closely related with urban thermal effects, surface temperature is widely investigated through establishing a general connection with city size. By taking other complex aspects of urban growth (e.g. spatial pattern, growth speed) into consideration, this study aims to provide a new and comprehensive evaluation of urbanization effect on local temperature change. Mechanical effects work through transforming flow patterns in urban areas, e.g. active turbulence is observed. More than focusing on turbulence itself in traditional investigations, this study attempts to explore the interaction between urban boundary turbulence and mesoscale weather, which is little understood before. The results would share new implications for local weather forecast.

Using satellite nighttime light for medium and large cities over eastern China, we quantitatively assess the rapid growth of urban areas and investigate its impact on long-term surface warming. Statistic results show that surface warming is closely related with the city size. More than city size, surface temperature increase also exhibits a strong association with urban growth. A rapid increase of surface temperature is observed mainly at cities undergoing rapid urbanization. On the other hand, a weak warming is reported at cities experiencing slow urban growth. Such a relation between urban growth and surface warming is evident over Central, South, and Northwest China, but it is weak over Northeast China, implying regional variations of temperature responses to urban growth compared with other region-dependent forcings (e.g. climate backgrounds and local features).

Satellite-derived land surface temperature analysis suggests the correspondence between urban growth and urban heat island expansion, which is then reflected by site observations. Cities experiencing rapid urbanization are more subject to the effects of urban heat island expansion, thus report strong warming. Isolated cities, which are far away from the rapid urban growth region, are less affected by the urban heat island expansion, thus experience weak warming. This strong link between temperature

trend and rapid urbanization explains the variations of warming rate among cities within the same region.

Mechanical effect of urban surface on flow structures is investigated by an urban-scale super high resolution simulation of a cold front passage over Guangzhou city, China. The flow structures differ dramatically between with-building and without-building experiments. In the presence of buildings, the cold front head moves at different speed thus deforms into an irregular line with bumps and dents at surface. At the top, cold front rises and falls alternatively due to different thermal patterns below it, and forms an undulating 3-dimensional structure. In general, the movement of cold front is slowed down over urban surface. Vertically, the cold front separates into upper and lower parts, with the lower part moving slower than the upper part due to the blocking effects of buildings. As a result, the air near the surface is warmer than its upper counterpart and forms a vertically unstable stratification favorable for turbulence generation. Consequently, active turbulence is identified over urban surface after front passage. The turbulence displays streaky structures and develops along streamwise direction. The streaky turbulence structures are most active above the building roof and have a horizontal scale of hundreds of meters, which is much larger than the building size.

Generation of the turbulence structures after front passage is closely related with the presence of buildings. Rising motion is formed behind buildings and developed along the downstream direction as a result of the warm air remaining after front passage. Sinking motion is then developed at neighboring areas as a compensation. With increasing contributions from shear and buoyancy production, the turbulent kinetic energy grows as cold front approaches. This energy reaches maximum value after front passage at a level above the building roof, supporting the development of organized turbulent structures.

The building-induced turbulence structures develop along the downstream direction and merge with front, resulting in the deformation of cold front. The rising motion of turbulence merges with the upward flow ahead of the front and strength, extending the strong rising flow to near surface. At neighboring areas, sinking motion

after front is intensified. They two together interrupt the front and generate an uneven front head compared with the condition when urban buildings are absent. The strong mixing within the front head also reduces the temperature gradient. The transformed flow structures express impacts on the transportation process. Turbulent Heat flux and momentum flux are locally strengthened by sweep and ejection events.

This study identifies the crucial contribution of surface warming induced by rapid urbanization to local temperature increase, thus pointing out the importance of urbanization complexity inherent in rapid growth in urban climate change over eastern China. These results provide a new view, which focuses on the rapid growth of urban, for evaluations of urban effects on local climate. Our high-resolution experiments focus on the turbulence in urban areas successfully extend previous street-scale investigations to city-scale studies and provide an example for studying urban boundary layer turbulence with real meso-scale weather and surface description. The results of our urban-scale building-resolving simulation reveal the possibility that cold front may be regulated dramatically after passing by an urban surface. The deformation of cold front is accomplished through the interaction between building-induced turbulence and front. Our results highlight that urban buildings may have significant impacts in regulating local weather.

Contents

Chapter 1 Introduction

1.1 Study background

Significant urbanization has occurred throughout the world during the past several decades. The urbanization process transforms farmland into concrete and buildings, which results in dramatic changes of the properties of the underlying surface. These changes show important influence of human activities on the local weather and climate (Collier, 2006). As urbanization continues, increasing populations are subjected to the changing urban weather and environments (Argueso et al., 2014). Elucidating the impacts of urbanization will have important societal implications.

Urban surface is characterized by obvious inhomogeneity. Large numbers of buildings with different heights and shapes intersect with streets, with a few parks embedded in. The complex urban surface modifies urban boundary layer structures and dynamics dramatically through thermal effects and mechanical effects (Roth, 2000; Martilli, 2002; Collier, 2006).

For the thermal effects, it evolves a huge release of anthropogenic heat in urban areas. The release of anthropogenic heat is related with population, energy use and other factors (Oke, 1988; Taha, 1997). In big cities like Tokyo, the magnitude of anthropogenic heat is about 200-400 W/m^2 and can reach a value as high as 1590 W/m^2 (Ichinose et al., 1999). This heat will be either directly released into the atmosphere thus affecting the heat flux or stored (Christen and Vogt, 2004). For the incoming solar radiation, large number of buildings will shadow, trap, and reflect the radiation within urban areas. And urban surface could store more heat due to high heat capacity compared with farm land. The warm urban surface will increase the release of long-wave radiation from land surface to atmosphere. Consequently, the surface heat budget over urban area is significantly modified.

Urban thermal effects influence surface temperature significantly. In cities, temperature increases much faster than climate background (Fujibe, 2009, 2011). Spatially, this difference of temperature trends displays an uniform distribution across the country (Kalnay and Cai, 2003). Positive difference is dominant at western coast of the US while positive and negative difference appear comparably in southeast part. This uniform distribution among various cities is said to be relevant with city size (Yang et al., 2011). Yang et al. (2011) indicates that metropolis record the strongest warming while small cities experience the slowest temperature increase compared with climate background. As a complex process, urbanization show complexity not only in urban size but also in other factors such as spatial patterns, growth speed. Because these complex aspects have impacts on local temperature as well, strong warming might be observed in some cities having a small population (Ren et al. 2008). Further elucidation of urbanization complexity which is rarely considered in previous evaluations and its impact on temperature trend will better clarify the urbanization effects on local climate change.

Urban mechanical effects tend to increase surface drag due to the presence of buildings. The few available urban observations illustrate a growing drag coefficient with an increasing surface roughness (Roth, 2000). The increased surface drag is usually accompanied by downward transport of momentum to surface (Roth, 2000; Kanda, 2006). A shear layer may be formed near the top of the buildings and convert mean kinetic energy into turbulent kinetic energy, which benefits turbulence generation (Roth and Oke, 1993; Roth, 2000).

Mechanical effects modify wind flow over urban areas and lead to various patterns according to urban morphology (Martilli, 2002). For example, strong sinking motion can be identified behind high buildings. While a calm zone may be generated among a cluster of buildings. Along the streets, horizontal wind may be strongly accelerated. More than surface properties, wind flow also varies significantly with weather conditions. Kim and Baik (2004) indicates that a small change of the inflow direction can lead to significantly different patterns of wind flow among buildings.

Consequently, reliable resolving of real surface and weather is strongly need.

Moreover, mechanical effects of urban buildings can significantly increase turbulence over urban areas (Bowne and Ball, 1970). As an important governing process, turbulent flow has been studied by observations and numerical simulations. However, traditional investigations usually focus on a small area such as several streets or a block, which may be affected by urban morphology. A large-scale study of turbulent, which can overcomes such influence, is a new challenge. Taking advantage of a large domain, interaction between turbulent over urban surface and mesoscale weather can be examined.

1.2 Purpose of the present study

In this study, we investigate urbanization impacts on local weather and climate from two aspects: thermal effect and mechanical effect. In chapter 2, we discuss about urban thermal effect on surface warming. By considering other factors of describing urbanization, which are little noticed before, a new quantitative evaluation of urbanization effect is proposed. Using this new-proposed measurement, we aim to clarify the role of urban growth in affecting local climate. In chapter 3, we focus on the mechanical effect of buildings on the turbulent structures over urban areas. Through extending previous street-scale studies to city-scale investigation, we try to provide a more general description of turbulent activities over urban surface. Taking advantage of our city-scale results, we pay special attention to the interaction between urban turbulent structures and mesoscale weather, which is difficult to be explored in previous block-scale studies.

Chapter 2 Role of rapid urbanization in surface warming over eastern China

2.1 Introduction

Urbanization entails dramatic changes of land surface properties and a huge release of anthropogenic heat that strongly affects the surface heat budget (Oke, 1988; Taha, 1997; Rizwan, Dennis and Liu 2008). It expresses an important influence of human activities on the local weather and climate. For instance, the urbanized area might induce an evident redistribution of temperature, humidity, winds, thunderstorms, rainfall and/or snowfall compared to their rural counterparts (Collier, 2006; Li et al., 2011). With urbanization continues globally, populations are increasingly subjected to the changing urban weather and environments (Argueso et al., 2014). Elucidating the impacts of urbanization will have important societal implications.

As a rapidly growing economy, China has undergone dramatic urban growth at large scale in recent decades. This region provides a good example for studying the urbanization processes and related impacts (Zhou et al*.,* 2004). Rapid urban expansion might engender the evident surface warming that has been detected since the early 2000s (Yang, Hou, and Chen, 2011). Because urbanization processes vary greatly over regions and over time, their impacts on surface temperature can be complex. For instance, temperature response to urbanization varies among city types (Ren et al., 2008). Cities with a larger population generally exhibit faster surface warming. More than city population, urbanization processes show complexity in spatial patterns, growth speed, and urbanization rates because of topographical limitations and local policy differences. Because these complex aspects have impacts on local temperature, strong warming might be observed in some cities having a small population (Ren et al., 2008). Further elucidation of urbanization complexity and its impact on temperature trend will clarify the urbanization effects on local climate change.

Previous studies have shed some light on the general relation between urbanization level and surface temperature change. Nevertheless, our understanding of the impacts of urbanization complexity remains limited. Over eastern China, an important feature of the complexity is the rapid growth of urban areas in recent decades. With the advent of remote sensing technology, high-resolution satellite night light imaging offers new opportunities to monitor urbanization processes (Welch, 1980; Sutton et al., 2001). In actuality, night light data have been used widely to identify urban areas over China (He et al., 2006; Ma et al., 2012; Wang et al., 2013). We infer that night light images can further facilitate quantitative assessment of rapid urban growth if both spatial and temporal variations are considered. Particularly, a long series of night light data enables us to link urban growth to surface temperature changes to ascertain its climate effects. This study describes our attempts to examine patterns of rapid urbanization (RU) and to clarify its impacts on surface warming over eastern China.

2.2 Data and methods

2. 2. 1 Data

Illuminated areas are good indicators of urbanized areas and urban population (Welch, 1980; Sutton et al., 2001). To resolve the detailed patterns and speed of urbanization, we use the cloud-free night light images provided by the Defense Meteorological Satellite Program Operational Linescan System (DMSP/OLS). This satellite product includes annual data of stable light from cities, towns, and other persistent light sources during 1992–2008. The light intensity is scaled as a digital number (DN) of 0–63, from dark to bright. With spatial resolution of 1-km, the night light images can well express the detailed urbanization patterns over China (He et al., 2006; Ma et al., 2012), as shown in Figure 2.1(*a*). In this study, we pay more attention to the increase of night light (Figure 2.1(*c*)) that relates closely to a change of population density, energy consumption, and land cover during the urbanization process.

The night light datasets come from five DMSP/OLS satellites: F10 (1992–1994), F12 (1994–1999), F14 (1997–2003), F15 (2000–2007) and F16 (2004–2008). An inter-calibration is needed to eliminate the systematic difference of satellites/sensors (Elvidge et al., 2009). Here, we estimate the annual composites for the cities over China and assume their mean difference at the overlapped years as the systematic differences. The composites from satellite F14 are used as the reference to adjust the imageries from other satellites. For those years when multiple satellites are available, an average of calibrated imageries is made and applied in further statistics. After calibration, the night light series becomes more continuous than the original one, and its trend is free from the effects of changing sensors (Figure 2.2).

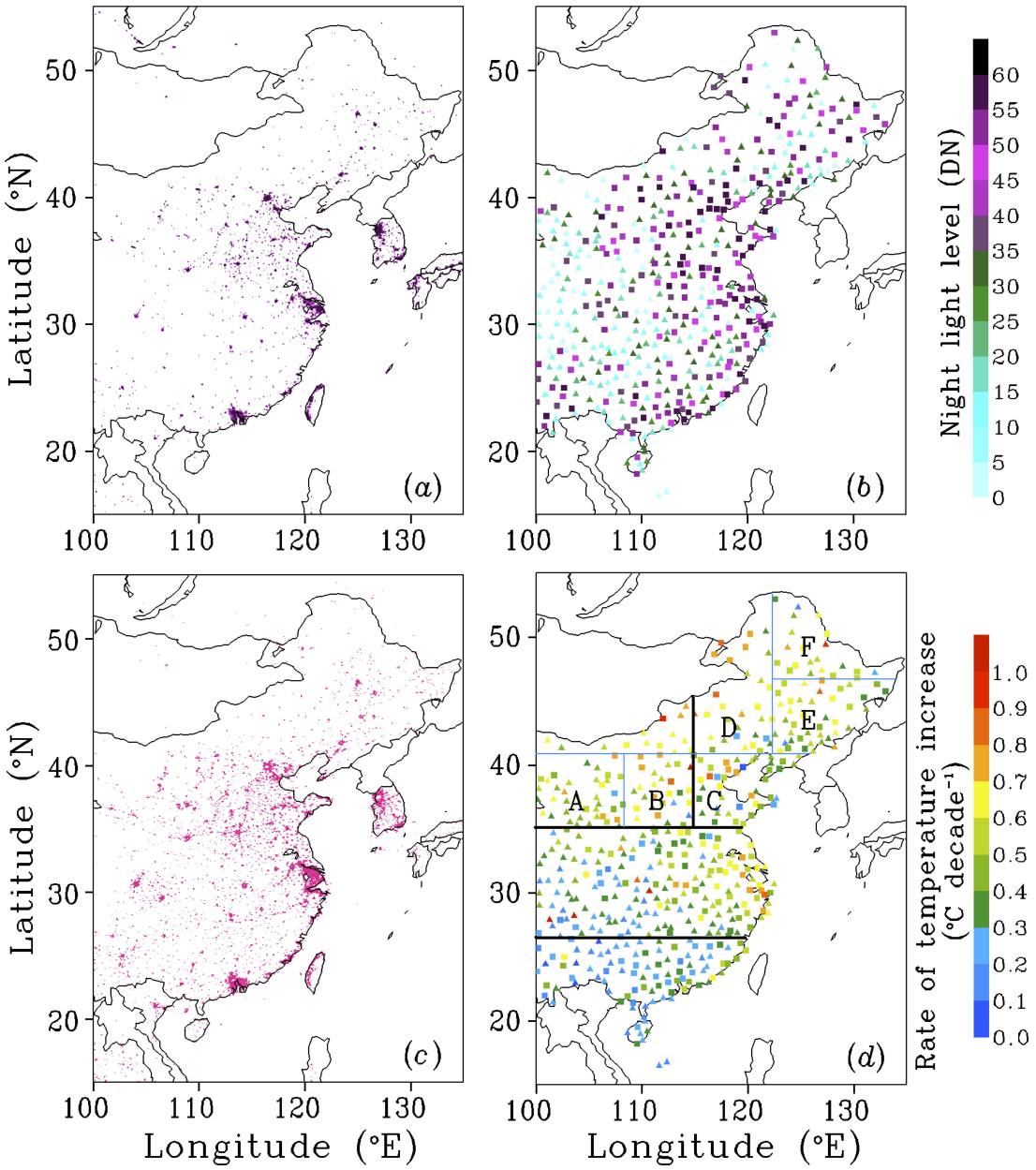

Figure 2.1 (*a*) Areas with night light DN ≥ 35 in 2008 according to DMSP/OLS data, (*b*) mean night light near CMA temperature-observation sites, (*c*) areas with a night light increase greater than 5 DN decade^{-1} during 1992–2008, and (*d*) surface temperature trend (°C decade^{-1}) during 1979–2008 estimated from *in situ* records. In Figures 2.1(*b*) and 2.1(*d*), triangles denote small cities/towns; squares denote medium/large cities. Four major subregions (Northeast China, Northwest China, Central China, and South China) are divided by bold lines in Figure 2.1(*d*) from north to south, which are applied in Figures 2.3-2.4. Northeast and Northwest China are further divided into six small domains (A-F) by thin blue lines, which are applied in Figure 2.6.

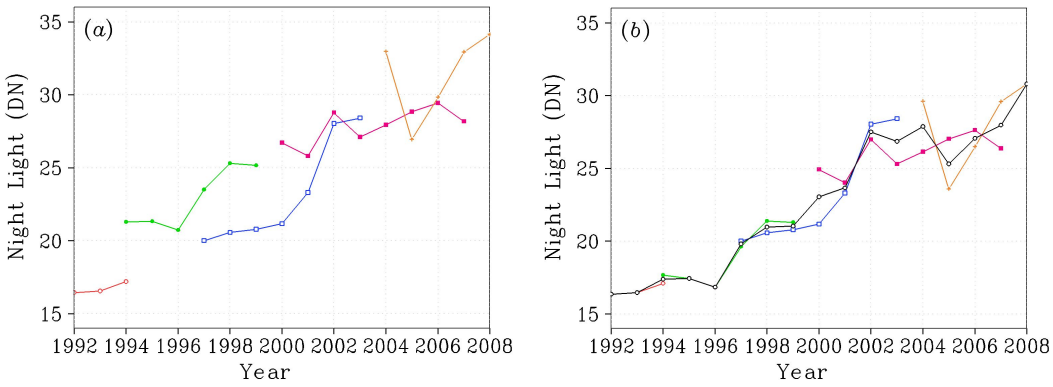

Figure 2.2 Time series of average night light over 486 observation sites in eastern China before (*a*) and after (*b*) calibration. The black line in Figure 2.2 (*b*) displays the average of calibrated series.

The long-term change of temperature over China is described using the monthly record of surface temperature from the China Meteorological Administration (CMA). These quality-controlled data are widely used to monitor the climate change over China (Zhou et al., 2004; Li et al., 2010). Over eastern China, surface temperature records are available over 486 sites in 1979–2008. By defining areas with night light DN $\geq$ 35 in 2008 as medium or large cities, 214 sites could be identified as being in medium and large cities, while other 272 sites are recognized as small cities and towns (Figure 2.1(*b*)). These definitions agree fairly well with the situation of Mainland China: there are around 30 provinces with each having one capital city and several major cities. We mainly focus on the medium and large cities where remarkable urbanization is likely undertaken. The temperature trend at each site is estimated using a linear regression model of the annual mean temperature. A few sites showing a negative temperature trend are neglected in this statistics, considering that they might be affected strongly by other irrelevant factors beyond the scope of this study.

To depict the physical processes involved, we examine the urban heat island to give more details on the RU impact at local scale. For the spatial pattern of temperature, we use the clear-sky land surface temperature (LST) derived from the Moderate Resolution Imaging Spectroradiometer (MODIS). The MODIS LST has a strong correlation with *in situ* air temperature and further allows us to define the

temperature distribution over urban areas (Hale et al., 2011; Tomlinson et al., 2012). The product MOD11C2 has a spatial resolution of 0.05° in longitude and latitude, which is high enough to resolve the local features of temperature. The temporal resolution of 8 days also offers many cloud-free samples to capture the well-defined pattern of urban heat island. The accuracy is better than 1°C (Wan et al., 2004). This accuracy is sufficiently good to resolve the temperature difference (approximately 4°C) between urban and rural areas (Jin, Dickson and Zhang, 2005). In this study, the LST difference between 2001 and 2008 are used to describe the urban heat island expansion in recent years.

2. 2. 2 Methods

a. Region division

Over China, the long-term change of surface temperature might vary among regions, arising from the different responses to topography, land cover, and climate background (Chao and Sun 2009; Yang et al., 2009; Ren et al., 2012). This regional difference of temperature change is less connected with urbanization effects. We suppose that surface warming recorded at observation sites can be divided into two components: one is contributed by large-scale warming such as global and regional warming, the other is affected by local forcings such as urbanization. In order to separate the temperature increase influenced by local forcings from the regional features of surface warming, we divided eastern China into four subregions (Figure 2. 1(*d*)): Northeast China, Northwest China, Central China, and South China. The divisions are similar to those used by Li et al. (2004), which are based on climatology analysis. We assumed that sites within the same subregion are subject to the same trend of the large-scale climate background, whereas their differences reflect impacts of local forcings, which varies with sites.

b. Measurement of urbanization effect

We then match up the night light images and surface temperature records to

describe the urbanization level and RU strength near observation sites. A moderate radius of 20 km, which is usually large enough to include one city but small enough to isolate it from neighboring cities, is applied in the match-up. It is noted that the results of present study are quite insensitive to this radius selection. The averaged contiguous night light value in 2008 within the 20-km radius from temperature observation site is used to designate the surrounding urbanization level. The average night light value is also a good indicator of city size and population (Welch, 1980; Sutton et al., 2001). To depict the urban growth, the long-term trend of night light is derived using a linear regression of the DN value at each 1-km^2 pixel. It is expected that, over the area under RU, night light undergoes an evident increase in satellite images. Here, a pixel with a light increase of more than 5 DN decade^{-1} is marked as a RU pixel. All RU pixels within 20-km radius from any given site are summed to obtain the RU area size. Consequently, the fast-growing urban areas are identifiable at a high resolution. The distance from the mass center of these RU pixels to observation site is also calculated. In this respect, both the spatial pattern of RU area and its relative distance to the observation sites can be estimated for all 214 medium/large cities over eastern China.

2.3 Results and discussion

2. 3. 1 Regional features of rapid urbanization and surface warming

Figure 2.1(*a*) displays the spatial distribution of night light (greater than 35 DN) over eastern China, implying the possible urban areas of medium and large cities. These illuminated areas account for about 1% of eastern China, suggesting limited coverage of medium and large cities. Aside from three major urban agglomerations (Beijing, Yangtze River Delta, and Pearl River Delta), numerous medium and large cities are scattered throughout eastern China. Figure 2.1(*c*) further portrays the region under RU, as indicated by shaded areas showing a rapid increase of night light (5 DN per decade or more). Compared with urban areas in Figure 2.1(*a*), the RU region has a wider coverage in Figure 2.1(*c*). It not only occurs at the medium and large cities but also appears in some small cities. Figure 2.1(*c*) shows that RU is significant at the three major urban agglomerations and other big cities such as the provincial capitals. Moreover, the scattered distribution of RU is dominant over the East China Plain (114−121°E, 30−40°N), corresponding to numerous medium cities there. Northeast China has fewer cities undergoing RU, yielding a sparse distribution of RU area in Figure 2.1(*c*). Such regional differences of RU reflect the uneven economic growth across China and underscore the complexity of urbanization.

The surface temperature trend during 1979–2008 over eastern China is shown in Figure 2.1(*d*). An obvious temperature increase occurs at most sites. On average, the surface temperature increase by 0.44°C decade^{-1} over eastern China. This increase is greater than the background increase of 0.33°C decade^{-1} estimated from NCEP-2 reanalysis data (Ma et al., 2008), which suggests that the surface warming recorded at most urban sites is stronger than the background climate change, highlighting an urbanization impact (Kalnay and Cai, 2003). Spatially, a fast temperature increase occurs in the northern regions of China (0.52°C decade^{-1} in Northeast China and 0.56°C decade^{-1} in Northwest China), whereas a slow warming trend appears over the southern region (0.26°C decade^{-1} in South China). These regional features illustrate the different responses of surface temperature to global warming, which is consistent

with previous studies (Li et al., 2004; Yang et al., 2009). As such large-scale patterns are less connected with local urbanization, we see a low correlation coefficient (0.24) between surface warming and night light for all sites across China.

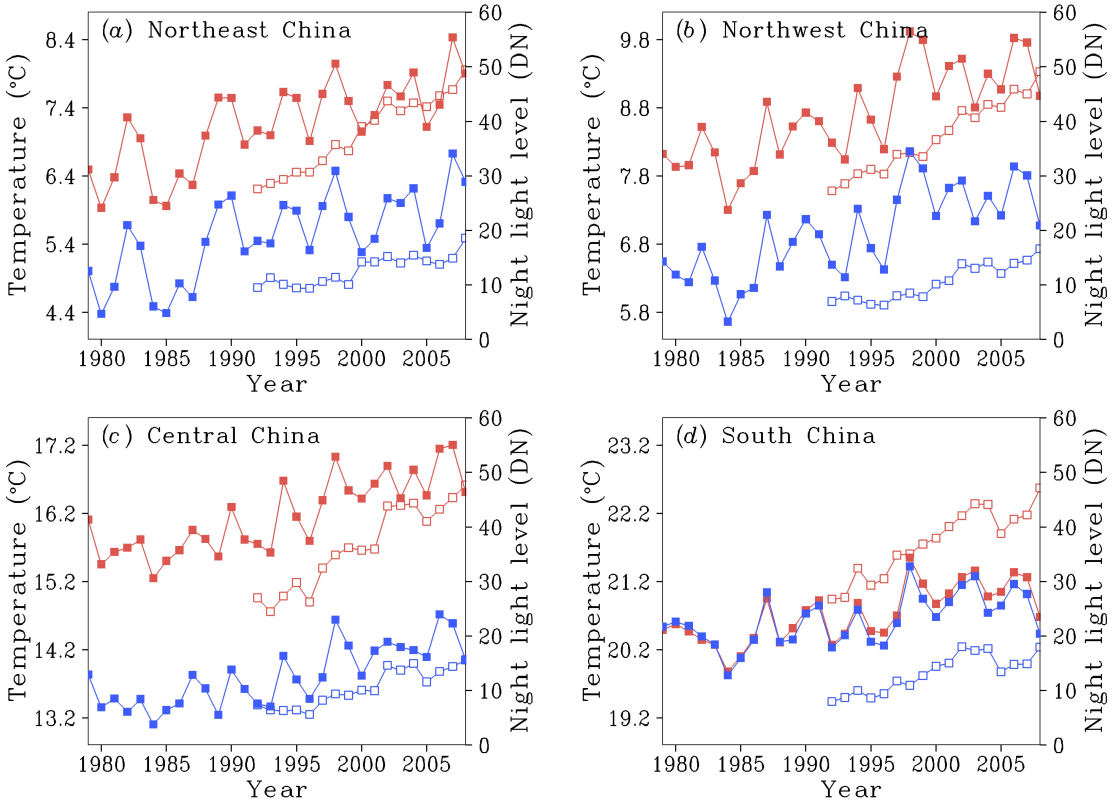

Figure 2.3 Inter-annual variations of the regional mean temperature during 1979-2008 (closed square) and night light during 1992-2008 (open square) at medium and large cities (red) and small cities and towns (blue) in four subregions of eastern China. The locations of four major subregions are shown in Figure 2.1(*d*).

To exhibit the urbanization process and related temperature change within each subregion, Figure 2.3 shows the interannual variations of regional mean surface temperature and night light in four major subregions. In Northeast China (Figure 2.3(*a*)), mean surface temperature is evidently high in the medium and large cities compared to the small cities and towns. The figure also shows that the rate of temperature increase is 0.55°C decade^{-1} in medium and large cities, which is slightly higher than that in the small cities and towns (0.49°C decade^{-1}). This result corresponds well to a more rapid increase of night light at the medium and large cities than in the small cities and towns. Similarly, in other three subregions, medium and large cities have a faster night light increase than the small cities and towns (Figures

2.3(*b*)–2.3(*d*)), indicating a stronger urbanization process. Correspondingly, a temperature increase of 0.61°C decade^{-1} is observed at medium and large cities over Northwest China, in contrast to that of 0.54°C decade^{-1} at small cities and towns. The temperature increase is 0.50°C decade^{-1} for the medium and large cities over Central China and 0.39°C decade^{-1} for small cities and towns. The temperature increase is 0.33°C decade^{-1} for the medium and large cities over South China and 0.24°C decade^{-1} for small cities and towns. Therefore, strong urbanization and surface warming mainly occurs in the medium and large cities across eastern China.

2. 3.2 Local features of rapid urbanization and its impacts on surface warming

Aside from the regional mean differences, the temperature trend is shown to vary considerably at sites within each subregion, despite having the same climate background (Figure 2.1(*d*)). For instance, over Central China, remarkable temperature increase is observed over the eastern part rather than the western part. This difference of surface warming within one region might be related to the difference of city size or urbanization speed. Figures 2.4(a)–2.4(d) shows that the night light level, which indicates the city size, has a mean value of 45–47 DN and a standard deviation of 7–9 DN over four subregions. It displays the various levels of urban development in the medium/large city sites over eastern China. Regression analysis results suggest that the warming rate generally increases with the city size. They exhibit a positive correlation in most subregions, except Northeast China. The highest correlation coefficient, 0.46, is found in Northwest China. This positive coefficient suggests that temperature increase tends to strengthen as the city grows larger. A good correlation between temperature trend and city size has been recognized in the previous studies (Oke, 1973; Yang et al., 2011), which employ urban population as a proxy of the city scale. Here, such a relation is also valid when using night light as the urban proxy.

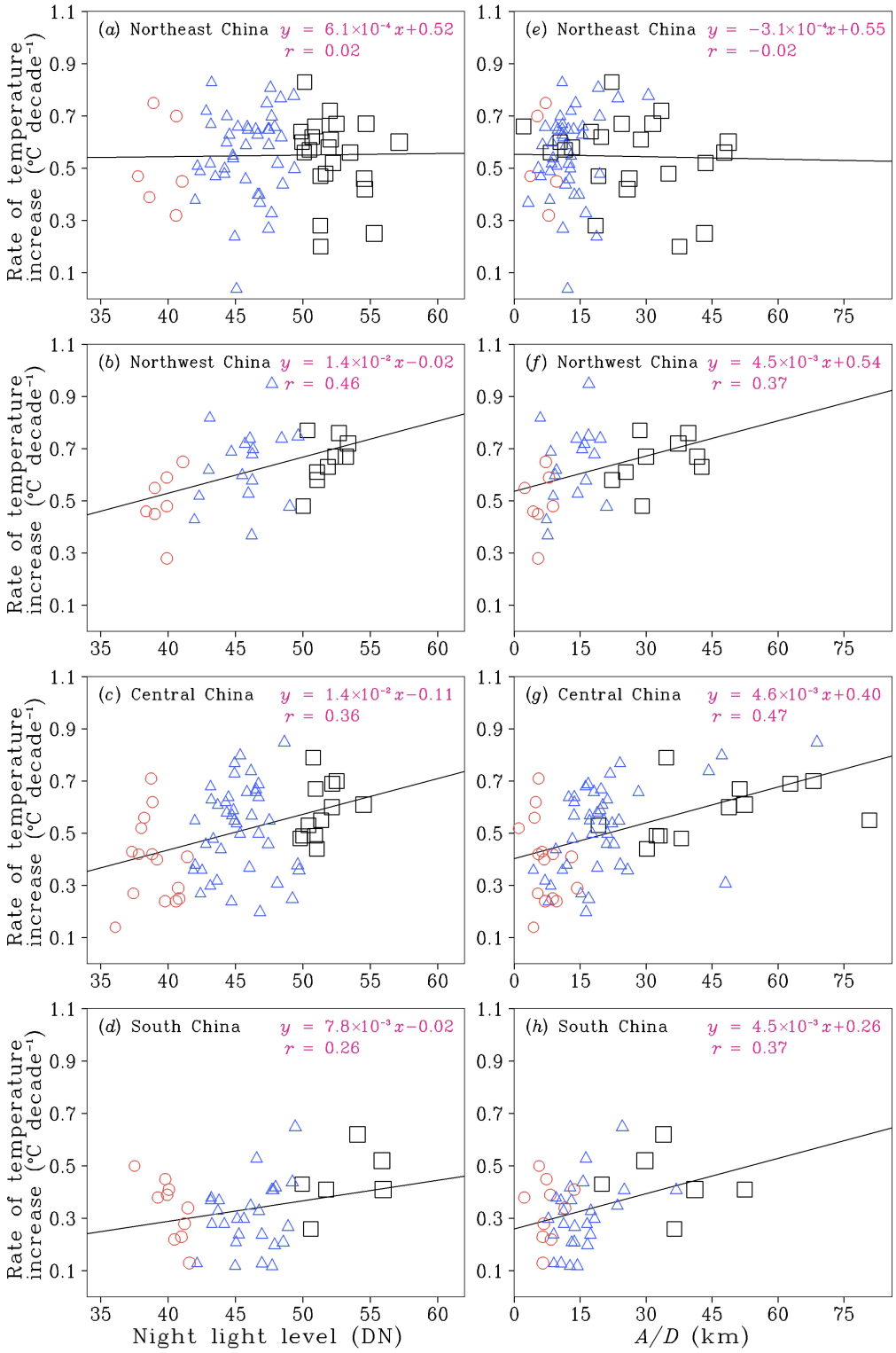

Figure 2.4 Scatter plots of the temperature trend versus average night light level (Figures 2.4(*a*)-2.4(*d*)) and rapid urbanization radius (Figures 2.4(*e*)-2.4(*h*)). Red circles, blue triangles, and black squares respectively denote the medium, large, and mega cities. Linear regression equation and correlation coefficient (*r*) are shown in the upper right corner of each figure. The solid line in each figure shows the regression line. The locations of these four major subregions are shown in Figure 2.1(*d*).

More than the city scale, we further specifically examine the speed and pattern of urban growth. The RU involves two major aspects: area (*A*) and distance (*D*) from *A* to observation site as indicated in Figure 2.5. It is reasonable to expect that, the larger the RU area size is, the stronger the influence on surface warming it might have. A distant RU area will have a weaker influence on an observation site. For any RU area, a newly grown RU pixel tends to increase the RU area size, but it has an impact on the mean distance depending on its relative location to the existing urbanized area and observation site. Therefore, a combination of area size and distance such as *A*/*D* might be defined to quantitatively measure the strength of RU near the observation site. It also can be viewed as an effective radius of RU ($R=A/D$, when D is not equal to zero). A larger value of *R* stands for a stronger RU strength with respect to the temperature-observation site.

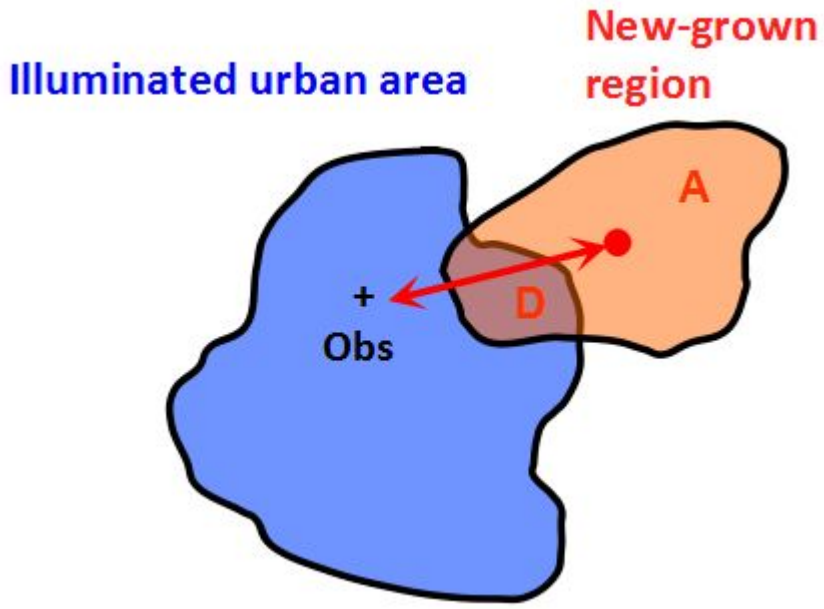

Figure 2.5 Schematic figure of the definitions of rapid urbanization area (*A*), distance (*D*). The cross mark (+) indicates the location of observation site. The blue area denotes illuminated urban area, which is usually used to stand for city size. The orange area indicates new-grown region defined by night light increase. The size of this area is the rapid urbanization area (*A*) used in our definition. The red dot is the mass center of rapid urbanization area, distance (*D*) is calculated as the distance between the mass center and observation site.

Statistical results show that the mean RU radius is 22 km for observation sites in Central China and 16–17 km for those in other subregions (Table 2.1). With the Yangtze River Delta and many scattered large cities, Central China has undergone faster urbanization than that in other subregions. The standard deviation of the RU radius is 17 km in Central China and 11–12 km in the other three subregions. Large value of standard deviation suggests that RU strength varies considerably in the cities in Central China, implying the local variations of urban growth. Furthermore, the RU radius is closely associated with city size. The correlation coefficient is approximately 0.8 in the four subregions, suggesting that stronger RU is more likely to occur in larger cities.

Table 2.1 Statistics of rapid urbanization radius (*R*), area (*A*), and distance (*D*) in four subregions over eastern China.

Region name	Mean R (km)	STD R (km)	Mean A (km2)	STD A (km2)	Mean D (km)	STD D (km)
Northeast	16.0	10.9	107.5	130.8	5.3	3.5
Northwest	17.1	11.7	114.7	138.2	4.8	3.4
Central	22.0	17.2	177.4	239.9	5.7	3.6
South	16.4	10.9	128.8	158.2	6.0	3.9

Figures 2.4(*e*)–2.4(*h*) show that the RU radius is strongly associated with the temperature trend in most subregions, except Northeast China. In general, cities with a larger RU radius record a faster temperature increase, whereas cities with a smaller RU radius display slower warming as shown by the regression trend. The medium cities usually have a small RU radius (<15 km) with small variation. Correspondingly, they report a small increase of surface temperature, suggesting a weak influence of RU. Large cities experience a strong urbanization, as indicated by the moderate RU radius mainly in a range of 5–25 km. Some show a RU radius larger than 20 km. These sites usually report a stronger warming trend than those having a comparable city size but a smaller RU radius. Mega cities display an even larger RU radius (usually larger than 30 km), which is generally accompanied by a faster rate of temperature increase than the medium and large cities. Most mega-city samples are

concentrated along the regression line, indicating that the temperature trend variation is closely related to the RU. All three types of cities (medium, large, and mega) together display a strong association between surface warming and RU. Given a positive correlation between city size and RU radius, it also suggests that the larger cities, which are more likely to experience stronger RU, tend to experience faster surface warming. This fact highlights that the RU expresses an important component of urbanization effects on local climate change.

Figure 2.4 shows that the relation between RU and temperature trend varies greatly in different subregions. The relation is most evident in Central China, with a correlation coefficient of 0.47 (Figure 2.4(*g*)), which is even higher than that between city size and temperature increase (0.36). In Central China, more sites are undergoing strong RU (with a RU radius greater than 30 km) than in the other three subregions. The temperature increase at these sites, irrespective of their city size, follows a close relation with the RU radius along the regression line. These sites display a higher warming rate than the sites with a small RU radius. Similarly in South China (Figure 2.4(*h*)), the temperature trend expresses a good relation with the RU radius. Their correlation coefficient reaches 0.37, which is higher than that between the city size and temperature trend (0.26). A significant urban effect on surface warming over southeastern China was found in earlier studies (Zhou et al., 2004; Yang et al., 2011). Here, RU is further identified as an important contributor during this process, as indicated by a strong link of RU and surface increase anomaly. The relation between RU and surface warming in Northwest China is also good (Figure 2.4(*f*)), with a correlation coefficient of 0.37. However, it is some lower than the correlation between city size and temperature increase (0.46). In Northeast China, although the medium and large cities tend to experience faster warming than small cities and towns (Figure 2.4(*a*)), details of the variations of warming rate among them are less linked to the city size (Figure 2.4(*a*)) or the RU strength (Figure 2.4(*e*)).

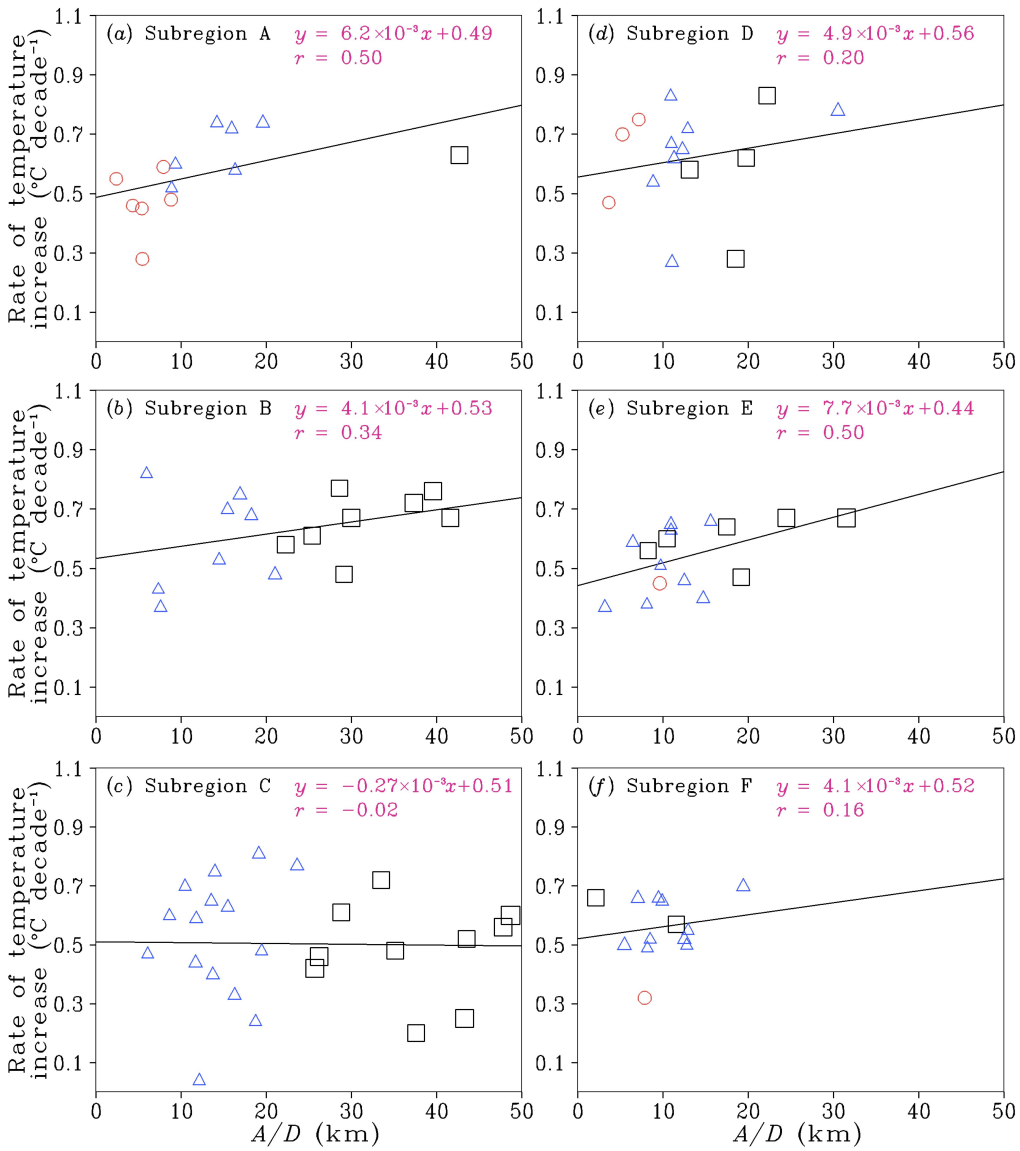

Figure 2.6 Same as in Figures 2.4(*e*)-2.4(*h*), but for the six small domains of northern China. The locations of these domains A-F are shown in Figure 2.1(*d*).

However, Figure 2.4 shows that the relation between surface warming and RU does not hold across the whole of China. It is less evident over northern China especially Northeast China. A weak relation between temperature trend and urbanization complexity over northern China is also noted in other reports (Li et al., 2004, 2010). It is speculated that the robustness of this relation may depend on the importance of urbanization relative to other forcings: large-scale climate change and regional features such as topography, land-sea contrast, and desertification (Xue, 1996; Wang et al., 2004; Chao and Sun, 2009; Li et al., 2010). To gain more insight into these processes, we examine RU and its relation with surface warming at more

specific regions. Northern China is further divided into six small domains A-F as shown in Figure 2.1(*d*). They roughly stand for the interior land, loess plateau, coastal zone, Inner Mongolia grassland, northeast plain, and northeast border, respectively. Figures 2.6(*a*)–(*c*) show that correlation coefficient for the cities at coastal areas (C) is evidently smaller than that at inland counterparts at the same latitude (A-B). Figure 2.6(*e*) show that the correlation between RU and temperature trend is good for the cities over northeast plain, where the industry is well developed. In contrast, the correlation is less evident for the cities at both Inner Mongolia grassland (Figure 2.6(*d*)) and northeast border (Figure 2.6(*f*)), where desertification and deforestation are severe (Xue, 1996). These results indicate that urbanization effect may be interrupted by the local features of land-sea contrast and land cover change, resulting to a loose relation between RU and surface warming. As shown in Figures 2.6(*c*)–(*f*), the response of surface warming to RU process can vary considerably among the subdomains of Northeast China. It seems to explain the low correlation over the whole region of Northeast China in Figure 2.4(*e*). This also reminds us to be cautious when attributing the variations of surface warming to RU, particularly at those regions where local features should be taken into account.

2. 3.3 Impacts of rapid urbanization on urban heat island expansion

To clarify how RU affects temperature records at local scale, we examine the spatial distributions of urban growth and urban heat island (UHI) in the Pearl River Delta, where RU has become evident in recent years. Figure 2.7(*a*) shows that the urban area expands considerably during 2001–2008. The urban areas change from isolated patches in 2001 to a contiguous pattern in 2008. Correspondingly, the area with warm anomaly detected by MODIS (an indicator of UHI) experiences an evident expansion (Figure 2.7(*c*)). Similarly, the city centers, as shown by the high values of night light, expand considerably during 2001–2008 (Figure 2.7(*b*)). The area of maximum UHI around city centers also expands correspondingly (Figure 2.7(*d*)). The good relation between urban expansion and UHI points to the importance of RU for temperature change. Over the Pearl River Delta, the UHI expansion might result from

a direct response of air temperature to land cover change from rice paddy fields to urban lands, as shown by a numerical study (Lin et al., 2007). Such a response usually involves the increased heat capacity of urban structure and the reduced evaporation (Argueso et al., 2014). Here, the observation evidence from satellite remote sensing supports this hypothesis.

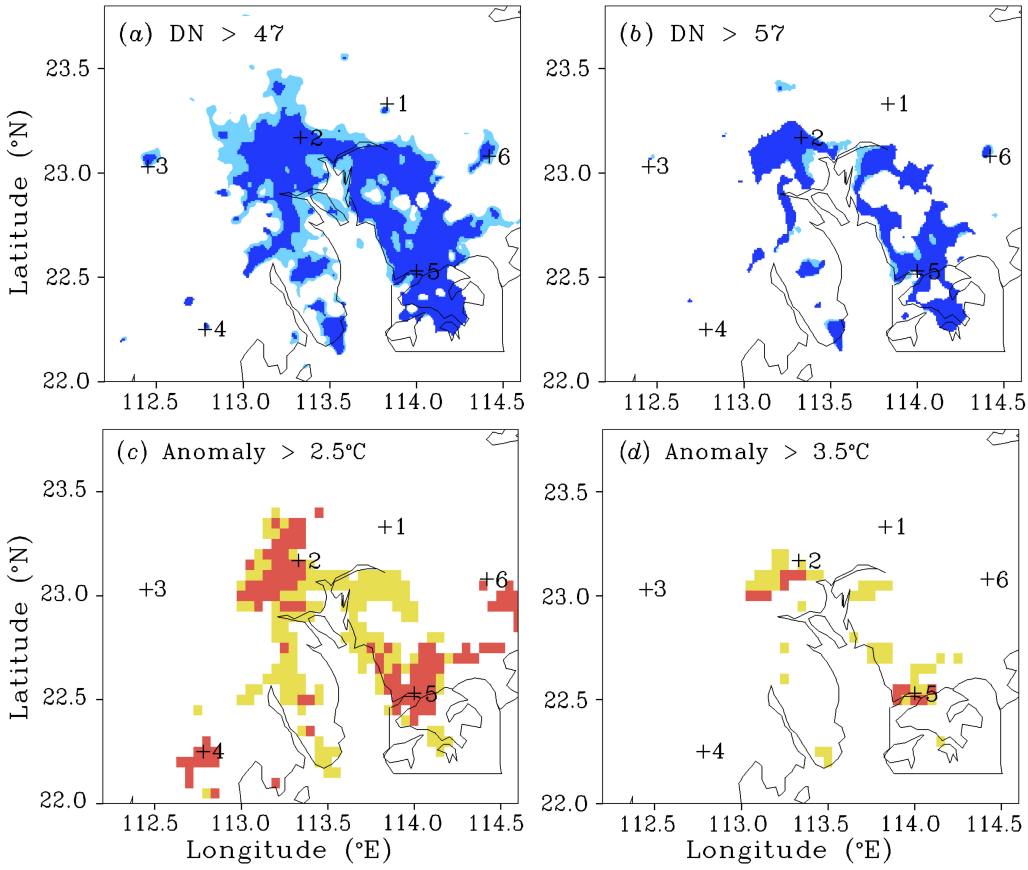

Figure 2.7 Illuminated areas over Pearl River Delta with night light DN above (*a*) 47 and (*b*) 57 according to DMSP/OLS. Dark blue areas show the coverage in 2001. Light blue areas show the expansion in 2008. The MODIS 8-day mean land surface temperature from 26 February with an anomaly larger than (*c*) 2.5°C and (*d*) 3.5°C. The red area shows coverage in 2001, and the yellow area shows expansion in 2008.

We further examine six cities in the Pearl River Delta to clarify the link between UHI expansion and temperature trend at the local scale (Table 2.2). Sites 2 and 5 are the two largest cities in the region. They have well-developed urban level (high average night light level) and marked urban area growth (RU radius greater than 29 km). Located in the coverage of UHI areas, they are clearly affected by the UHI expansion induced by RU (Figures 2.7(*c*)–2.7(*d*)). Correspondingly, they experience

strong surface warming up to 0.41°C decade^{-1}. Although site 6 is located near a small city, it experiences considerable urban growth with the RU radius of 36.9 km. A strong temperature increase of 0.41°C decade^{-1} is reported there, which is comparable to that observed in large cities (sites 2 and 5). Sites 1, 3, and 4 are located in cities that undergo slow urbanization (with RU radius of 8.9−13.7 km). They are also distant from the coverage of UHI areas and are therefore less affected by the UHI expansion. They report a weak surface temperature increase (0.21−0.37°C decade^{-1}). Therefore, we see clearly that the variations of the surface warming rate at local scale might result from the temperature response to the UHI expansion induced by rapid urban growth over Pearl River Delta. Similar results are also seen in other regions that exhibit a strong relation between RU and surface warming (Tables not shown).

Table 2.2 Urbanization parameters and temperature trends at six observation sites over the Pearl River Delta.

Site No.	City name	Night light level (DN)	RU area (km^2)	RU distance to observation site (km)	RU radius *A*/*D* (km)	Rate of temperature increase (°C decade^{-1})
1	Zengcheng	45.3	47	5.3	8.9	0.24
2	Guangzhou	56.0	610	14.8	41.1	0.41
3	Gaoyao	48.5	124	9.1	13.7	0.21
4	Taishan	43.8	36	3.3	10.6	0.37
5	Shenzhen	55.9	409	13.8	29.7	0.52
6	Huiyang	47.8	397	10.8	36.9	0.41

Notes: Site locations are marked as described in Figure 2.7. *A* is the area of RU, and *D* is the mean distance from *A* to observation site.

2.4 Summary

In this study, the impacts of rapid urban growth on surface warming have been investigated using a long archive of surface temperature data and satellite night light images. A quantitative estimate of the RU strength is assessed using the area size of the rapid night light increase and its distance to observation sites. Results show that the surface warming is occurring to a great degree at sites that have undergone rapid urban growth. Such a relation is more likely to occur in large and mega cities. The rapidly intensifying urban warming at large and mega cities is therefore contributed by an enhanced temperature trend because of RU. This relation is most evident in Central and South China, but it varies considerably in northern China, possibly because of the different temperature responses to urbanization effect relative to other climate forcings. Analysis of satellite-derived surface temperature suggests that RU is generally accompanied by an expansion of urban heat island. The sites affected by RU-induced UHI expansion tend to experience strong warming. In contrast, for sites far away from RU, they are less affected by the UHI expansion and thus report weak warming. Such a strong link between temperature trend and RU at both regional and local scales is supportive to attributing increased temperature anomaly to rapid urban growth. These results also point to the fact that the urban climate change over eastern China might include an important component of surface warming induced by RU.

Urbanization effect is an important contributor to increase regional surface temperature (Ren et al., 2012; Qiao, Tian and Xiao, 2013). It accounts for about 40% of overall surface warming, and might exceed 50% in some regions throughout China (Zhou et al., 2004; Ren et al., 2008; Yang et al., 2011). The results of this study suggest that urban warming might be related to urbanization complexity inherent in rapid growth. The complexity might help describe the urbanization process precisely and lead to a good evaluation of urban effects on local climate. This study mainly examines the urban impacts at the medium and large cities because of data limitation. It is recognized that small cities also experience urban growth on a local scale (Karl, Diaz and Kukla, 1988; Yang et al., 2011). With high-resolution observations

monitoring both temperature and urban expansion, additional studies must be undertaken to clarify the impact of urbanization complexity on temperature trends in cities of various scales. As urbanization expands throughout the world, it is also expected that urbanization complexity might affect the surface temperature change in other countries and regions. The relation between surface warming and RU might differ among countries and regions just as it performs variously among the subregions over China. Implications of such regional variations are that the response of surface warming to RU might vary according to the climate backgrounds and local features (topography, land-sea contrast, desertification, deforestation, etc.). Therefore, the region-dependent climate forcings should be further considered when evaluating the temperature change caused by RU in different regions.

Chapter 3 An urban-scale high resolution simulation of turbulent structures during a cold front passage

3.1 Introduction

Urban mechanical effect could modify wind flow as well as urban boundary layer structure dramatically (Roth, 2000; Collier, 2006). One important modification is the increased turbulence intensity and shifted maximum intensity wavelength over urban areas (Bowne and Ball, 1970). Turbulent flow is one of the crucial governing processes of exchanges of mass, momentum and heat between urban surface and atmosphere. It also displays important impacts on energy balance and pollutant dispersion. Better knowledge of urban boundary layer turbulence will have important societal implications.

Although turbulent flow appears instantaneously, it contains spatially coherent motions which distributed regularly. Both observational and numerical investigations point out the existence of organized turbulent structures (Schols, 1984; Roth, 2000; Kanda, 2006; Inagaki et al.,2011). The structures display various features under different weather conditions (Moeng and Sullivan, 1994; Khanna and Brasseur, 1998; Foster et al., 2006; Park and Baik, 2013). The organized structures also vary with surface geometry (Kanda, 2006; Park and Baik, 2014). Thus reliable resolving of real surface and weather conditions can significantly benefit a better description of turbulent structures in real case experiments.

Previous observational and numerical studies provide valuable understandings on the features and generation of turbulent organized structures. Considerable field observations have been carried out in order to investigate the turbulent structures in urban boundary layer (Schols, 1984; Roth and Oke, 1993; Oikawa and Meng, 1995). These field observations usually use point or tower measurements. Limited observations confine these studies to a specific setting of urban morphology and

surface condition, thus reduce the generality of the results. Similarly, most numerical studies employ a small domain at street or block scale (Kanda et al., 2004; Baik and Park, 2009; Inagaki et al., 2011). It is also noted that in the numerical simulations urban buildings are represented by idealized setting of blocks at most times (Kanda et al., 2004; Inagaki et al., 2011; Park and Baik, 2013). Large scale simulations, such as a whole city scale, with real configuration of urban buildings are sparse.

Moreover, the linkage between local urban weather and mesoscale weather is not well established. On one hand, mesoscale weather affects local weather. For example, the occurrence of land-sea breeze would decrease temperature over urban areas, change the pattern of air-pollutant distribution as well as modify the boundary structure (Tsutsumi et al., 1990/91; Melas et al., 1995; Liu and Chan, 2001). On the other hand, urban weather also expresses its impact on mesoscale weather. Urban surface can modify rainfall development and lead to a redistribution of precipitation pattern at meso scale (Thielen et al., 2000; Rozoff et al., 2002; Guo et al., 2006; Zhong and Yang, 2015). These valuable insights suggest the possible interaction between urban surface and mesoscale weather. However, details of this interaction is little investigated. In particular, the interaction between urban turbulent structures and mesoscale weather is unknown.

In the present study, an urban-scale numerical simulation at super high resolution is performed. This urban-scale modeling focuses on a cold front passage over Guangzhou city, China. Special attention is paid to the interaction between urban-induced turbulence and cold front. By using the simulation results, this study aims to clarify the turbulent organized structure and its impact on cold front.

3.2 Model description and experiment design

This section describes the Down-Scaling Simulation System (DS^3) used in the present study. This system is designed for a super high resolution forecast of mesoscale weather. The DS^3 combines a parallelized CFD model with a mesoscale model through one-way nesting. Such kind of coupled CFD model and meoscale model is proved to be capable of simulating the wind field at high resolution (Chen et al., 2015).

3.2.1. Numerical modeling system

In this study, the super high resolution simulation is carried out by DS^3. The detailed configuration and verification of DS^3 is described by Chen et al (2015a, b). The flowchart of DS^3 is shown in figure 3.1. First, a mesoscale model is used to simulate the real weather conditions at synoptic scale. The model employed is the Japan Meteorological Agency Non-Hydrostatic Model (JMA-NHM) (Saito et al. 2006, 2007). Then the results are downscaled into local scale reaching cloud-resolving resolution. By this means, real mesoscale weather can be described with reasonably good accuracy. Then the downscale results are used as the initial condition to drive a building-resolving CFD model (Sha et al., 1991; Sha 2002, 2008). Detailed configuration of the CFD model is shown in Table 3.1. In the CFD model, topography and urban buildings are explicitly described at a building-scale resolution. Thus the impacts of urban buildings can be expressed clearly. In this respect, the mesoscale simulation of local weather can be achieved at super high resolution, which means it is able to resolve each building over a whole city.

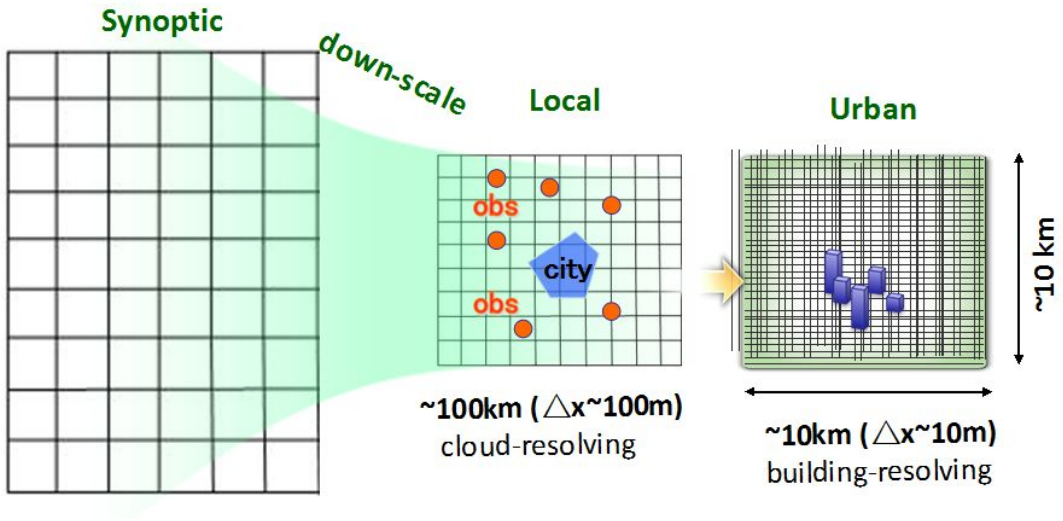

Figure 3.1 Flowchart of the Down-Scaling Simulation System (DS^3).

Table 3.1 Configuration of the CFD model SIMPLERgo

Model parameters	Specifications
Basic equations	Non-hydrostatic (compressible)
Coordinate	Three-dimensional Cartesian
Discretization approach	Finite volume method
Grid system	Staggered
Spatial resolution	Adaptive/uniform
Time integration scheme	Fully implicit
Advection Scheme	3rd upwind scheme (QUICK)
Equation solver	SIMPLER algorithm
Surface geometries treatment	Blocking-off method
Turbulence scheme	Lilly-Smagorinsky LES model

3.2.2. Experiment design for the cold front event

In the downscale simulations of JMA-NHM, four domains are employed (Figure 3.2). The domain settings are described in Table 3.2. The outer domain (D1) starts from southern China (Figure 3.2 (a)) with a resolution of 15 km. Following by domains with resolutions of 2 km and 400 m, a resolution of 100 m is achieved at the fourth domain (D4, figure 3.2(d)).

Table 3.2　Model settings of downscale experiments in JMA-NHM

Model	JMA-NHM			
Domain	D1	D2	D3	D4
Horizontal resolution	15 km	2 km	400 m	100 m
Time step	60 s	6 s	2 s	2 s
Horizontal grid number	80×80	80×80	80×80	120×120
Vertical layer	50	50	50	50
Initial condition	NCEP (6hourly, 1.0 deg)	Results of D1	Results of D2	Results of D3
Cumulus parameterization	Kain-Fritsch Scheme	none	none	none
PBL scheme	MYNN3			

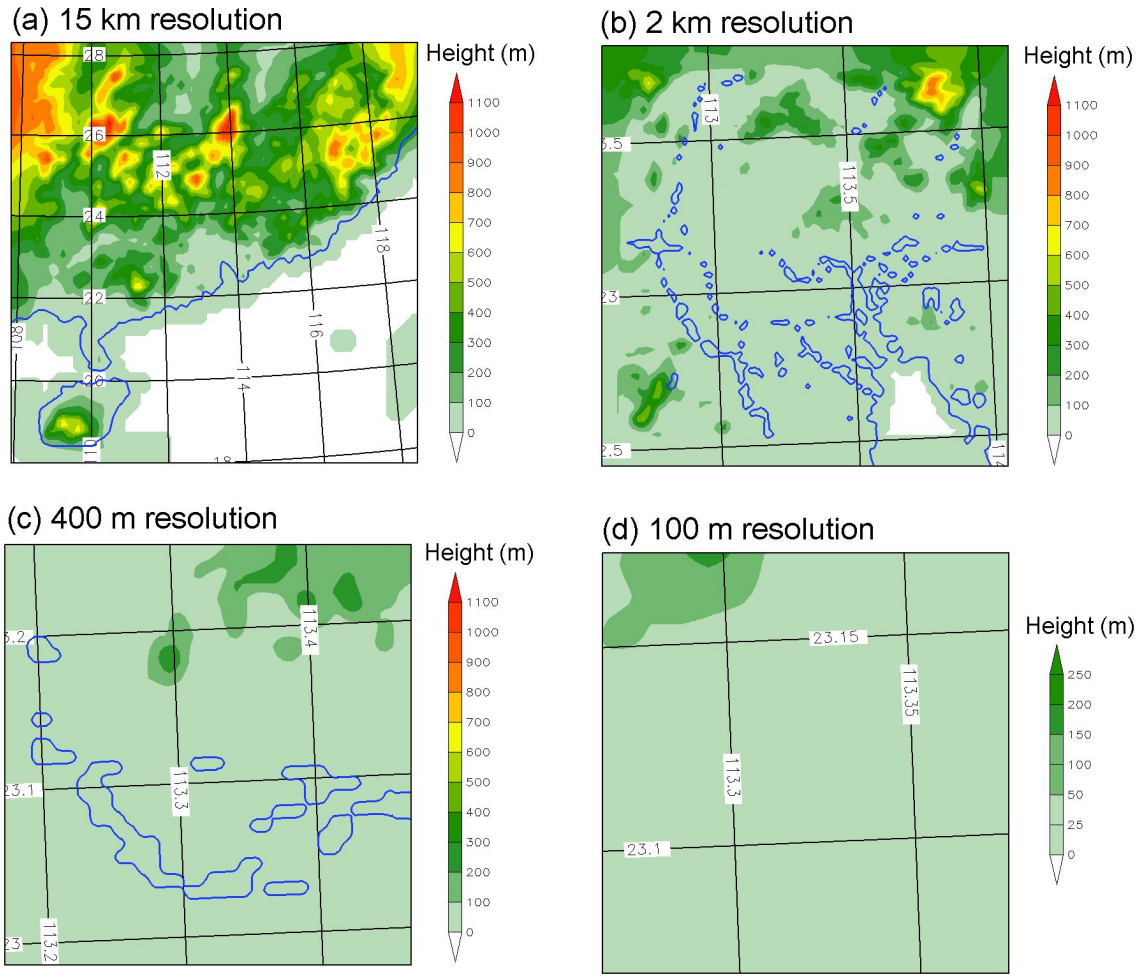

Figure3.2 Domain settings of the downscale simulations in the JMA-NHM. Figures 3.2(a) - (d) show the calculation domains of 15 km-resolution, 2 km-resolution, 400 m -resolution, and 100 m-resolution simulations respectively.

In this study, we focus on the impacts of urban surface. Two experiments are designed in the CFD simulation (Figure 3.3). Both experiments employ a 10-km domain with a resolution of 10 m. In the BLD experiment (Figure 3.3(a)), real buildings as well as topography are incorporated into the CFD simulation. In the TOPO experiment (Figure 3.3(b)), only topography is considered. By comparing the two experiments, the impacts of buildings on the flow structures are clear.

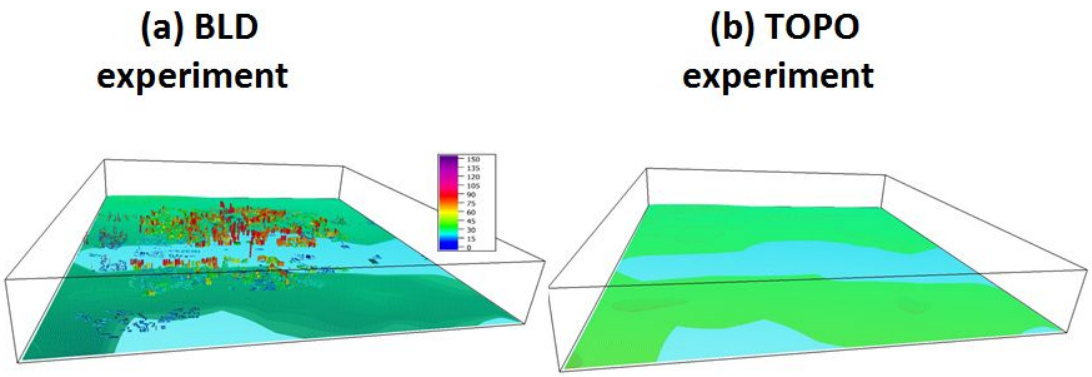

Figure 3.3 Domain settings of the CFD simulations. Figure 3.3(a) indicates surface configuration of both building blocks and topography, figure 3.3(b) indicates only topography surface.

3.3 Observation of the front passage

ERA-Interim reanalysis data show that cold front passed Guangzhou city around 06:00 (UTC) on Dec.29, 2012 (Figure 3.4). The location of cold front is denoted by dense temperature gradient, which indicates a more than 10 ℃ temperature difference before and after cold front. Surface wind also displays significant difference before and after cold front. Before front, surface wind is dominant by east wind from the sea. The wind speed is low in the continent especially near front. After front, strong surface wind from north is the main feature.

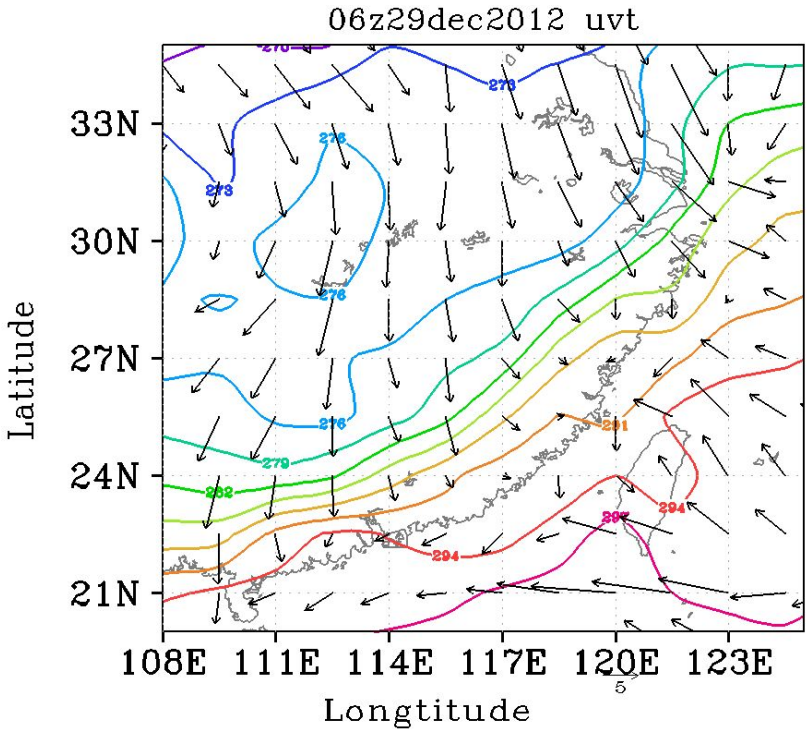

Figure 3.4 ERA-Interim surface horizontal wind (vector) and temperature (contour) at 06:00 (UTC) 29 Dec, 2012

Surface observation at Guangzhou city also recorded the cold front passage. At that day, surface temperature decreased rapidly from 19℃ to 10℃ (Figure 3.5(a)). At the same time, wind direction changed from 90 degree (east wind) to 360 degree (north wind), accompanied with an significant increase of wind speed from 2 m/s to 8 m/s (Figure 3.5 (b), (c)). These changes which happen rapidly are correspondent with the horizontal features shown in figure 3.4.

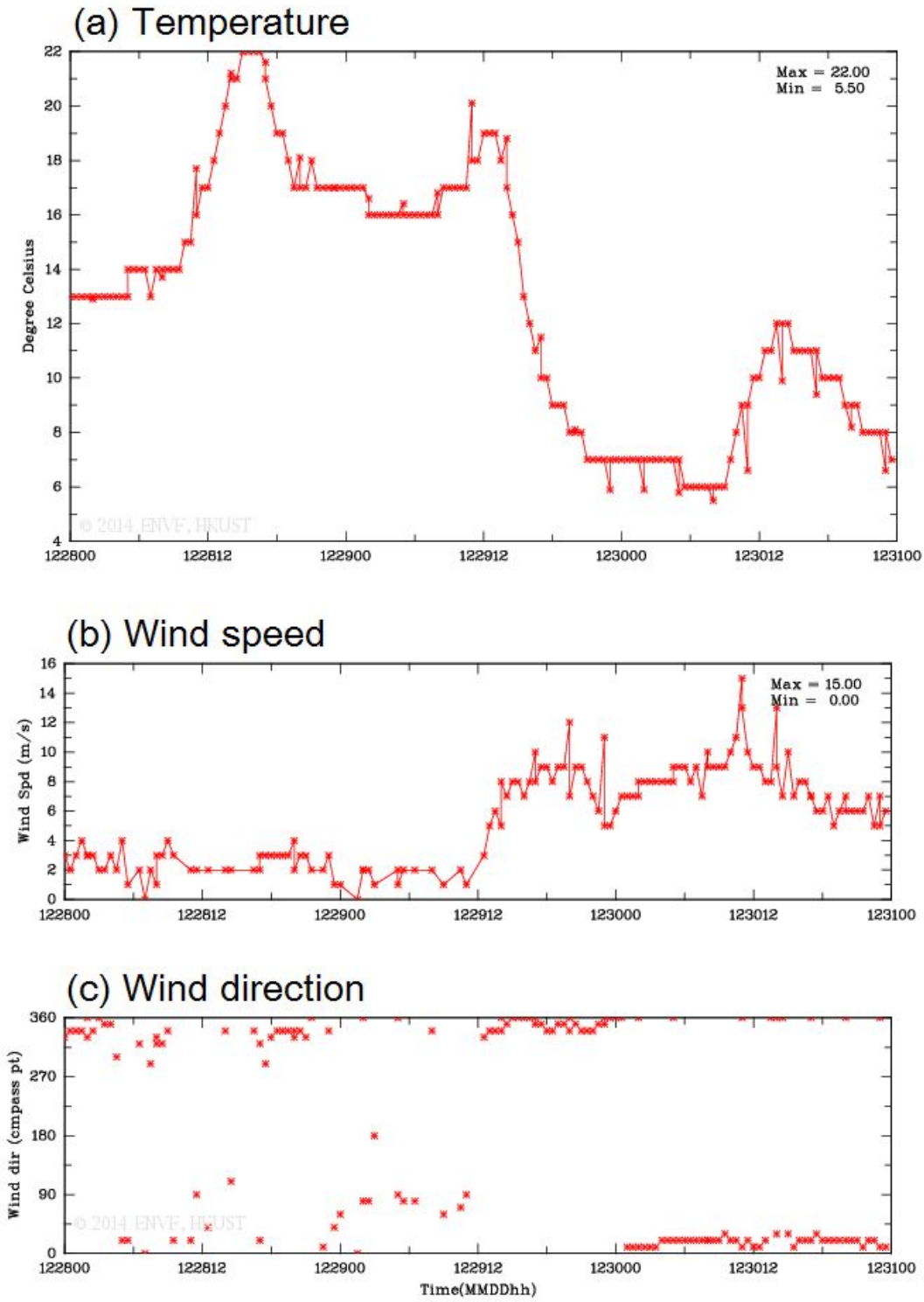

Figure 3.5 Surface observation of (a) temperature, (b) wind speed, and (c) wind direction at Guangzhou city during 28th-31th Dec, 2012.

3.4 Overall simulated front structures

3.4.1 Horizontal distribution

Cold front invades into Guangzhou city from northwest. Horizontal wind changes from southeast to northwest, accompanied with a significant increase of wind speed. Strong rising motion is identified before the front line, followed by sinking motion after front.

The cold front pattern differs dramatically between with and without buildings experiments. In the presence of buildings, cold front is deformed by urban surface and evolved into an irregular line with localized rising and sinking motion (Figure 3.6(a)). The front line is regulated and forms several bulges and indentations. Updrafts ahead of front are strong at the areas where cold front is recessed. As a comparison, cold front is smooth and regular in TOPO experiment (Figure 3.6(b)). The front line displays an arc shape. Ahead of cold front, uniform strong rising motion is aligned. Weak sinking motion appears after front.

It is also noted that front movement is slower in the BLD experiment than in the TOPO experiment as indicated by the location of front line. For example, at the location x=6 km, cold front locates at around y=5 km in the BLD experiment. While cold front locates at around y=3 km in the TOPO experiment. The retarded front over urban surface is probably due to the blocking effect of urban surface as well as the interaction between urban buildings and cold front.

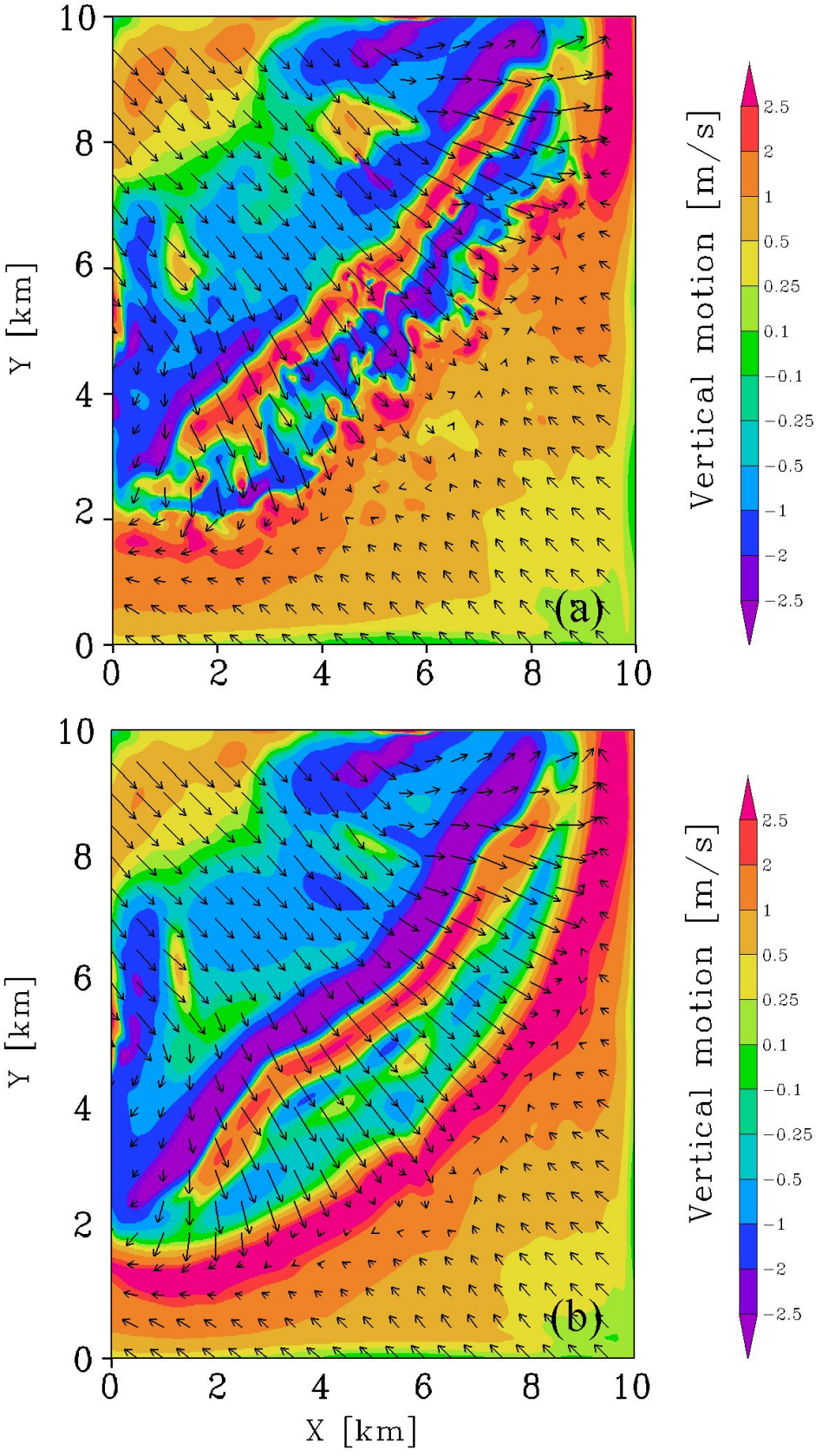

Figure 3.6 Horizontal distribution of uv wind (vector) and vertical motion (shade) in BLD (a) and TOPO (b) experiment at ft=600s at z=350m.

Time evolution of temperature and wind speed at the central grid also reveals slower movement of cold front over urban surface compared with topography surface (Figure 3.7). At the beginning, temperature records from two experiments are same. Temperature in the TOPO experiment begins to decrease rapidly around 380 s and reaches minimum at around 440-450 second. After that, it starts to increase slowly. In the BLD experiment, temperature drops rapidly from about 400 s, which is 20 seconds later than that in TOPO experiment. Temperature ends the rapid falling at around 520 s and almost keeps the same value from that time. Similarly, wind speed from two experiments experience a slow decrease samely at the beginning. Then wind speed in TOPO experiment reaches the bottom first and starts a rapid increase. Wind speed in BLD experiment reaches minimum value 20-30 seconds later and begins to rise rapidly. The postponed decrease of temperature as well as increase of wind speed in BLD experiment compared with TOPO experiment indicate the delayed passage of cold front over urban surface.

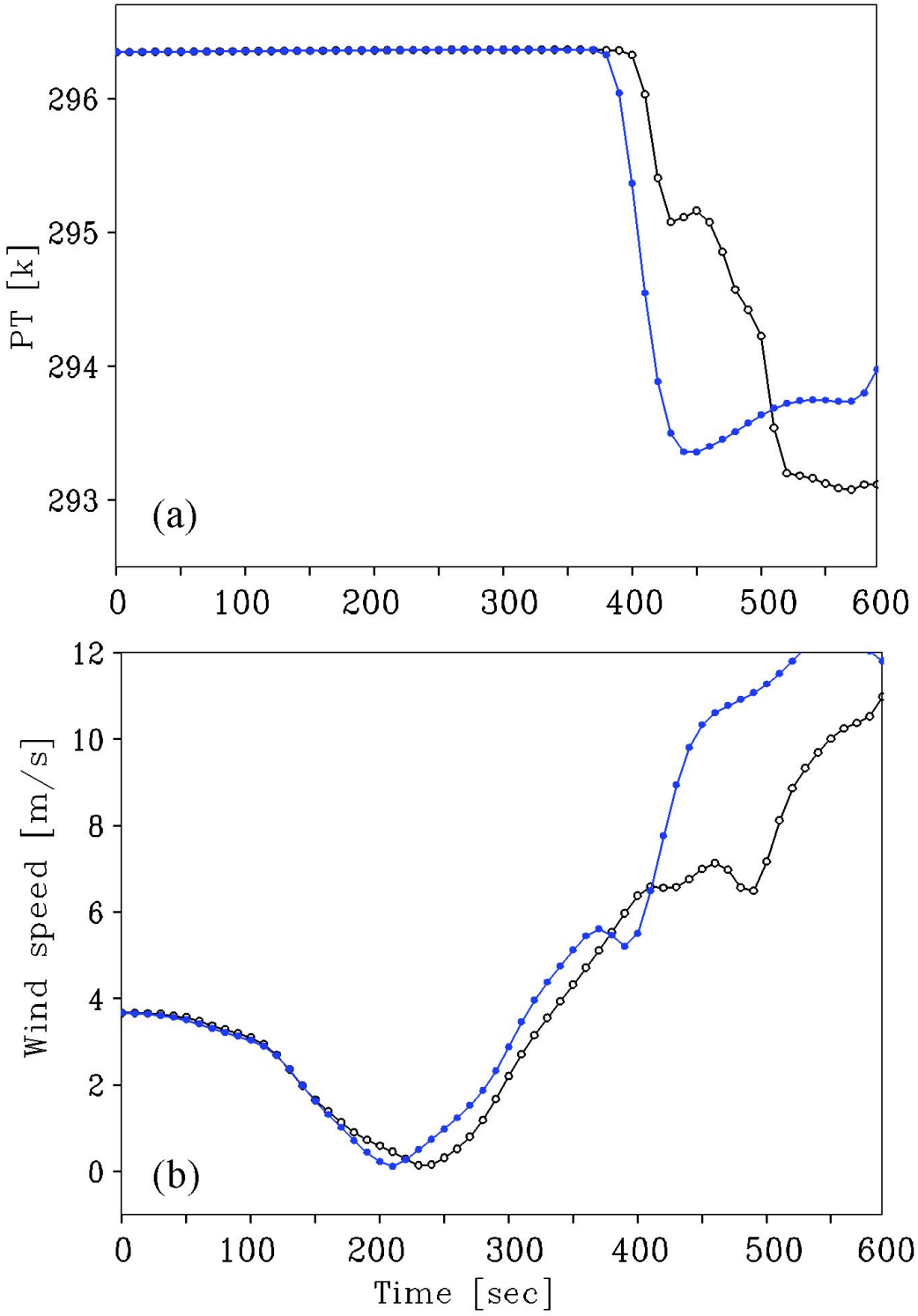

Figure 3.7 Time series of temperature (a) and wind speed (b) at z=360 m. Blue lines indicate time evolution in TOPO experiment, black lines indicate time evolution in BLD experiment.

3.4.2 Vertical structure

The vertical structure of cold front is examined in two experiment (Figure 3.8). The cold air mass moves as an unity when there are no buildings (Figure 3.8(b)). In contrast, cold front separates into upper and lower parts (Figure 3.8(a)) in the BLD experiment. The lower part moves slower than the upper part due to the blocking effects of buildings. As a result, the air near the surface is warmer than its upper counterpart as shown in figure 3.8(c). In front head, air mass near surface can be 1-3 K warmer than its upper counterpart. This warm difference is mainly appeared below 200 meter. Such a vertically unstable stratification is favorable for turbulence generation.

3.4.3 3-Dimension front structures

Figure 3.9 shows 3-dimensional isosurface of temperature in two experiments. The thermal structures of cold front are corresponded with the vertical motions shown in Figure 3.8. Over urban surface, cold front head is regulated dramatically by buildings and forms 3-d structures (Figure 3.9(a)). The isosurface displays an irregular shape at surface, with some areas protrude and some areas recess. These bulges and indentations indicate various speed of front movement over urban surface. At the top of front head, the isosurface rises and falls alternatively, forming a undulating cold front head. The ups and downs suggest different thermal patterns at different areas. Below the rising isosurface, temperature is higher than neighboring area as indicated by the empty holes of the isosurface. While below the sinking isosurface, temperature in lower than near-by area. It is also noted that the isosurface near surface protrudes from cold front below the sinking areas at the top. The bulging isosurfaces suggest a rapid advance of cold air mass over these areas.

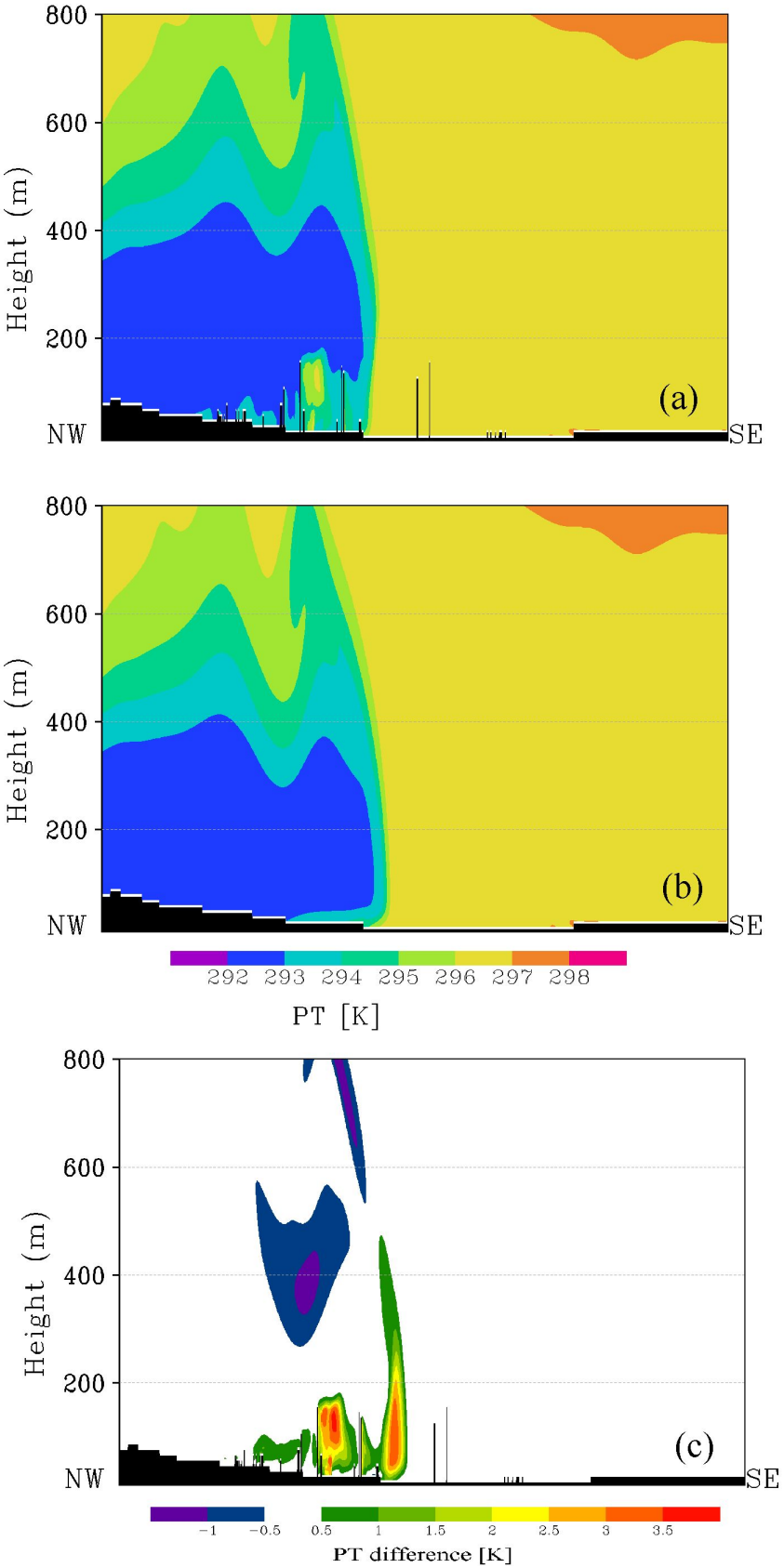

Figure 3.8 Vertical thermal structure of cold front head at ft=320s in BLD (a) and TOPO (b) experiment. Figure 3.8(c) shows the temperature difference between TOPO and BLD experiments.

In comparison, cold front head displays 2-d structures when urban buildings are absent (Figure 3.9(b)). The isosurface is regular at surface with a arc shaped front line, suggesting a uniform speed of front movement over the whole domain. The isosurface of cold front head is smooth compared with that over urban surface. The smooth distribution of temperature illustrates the 2-d front head structure, which keeps consistent in the front line direction.

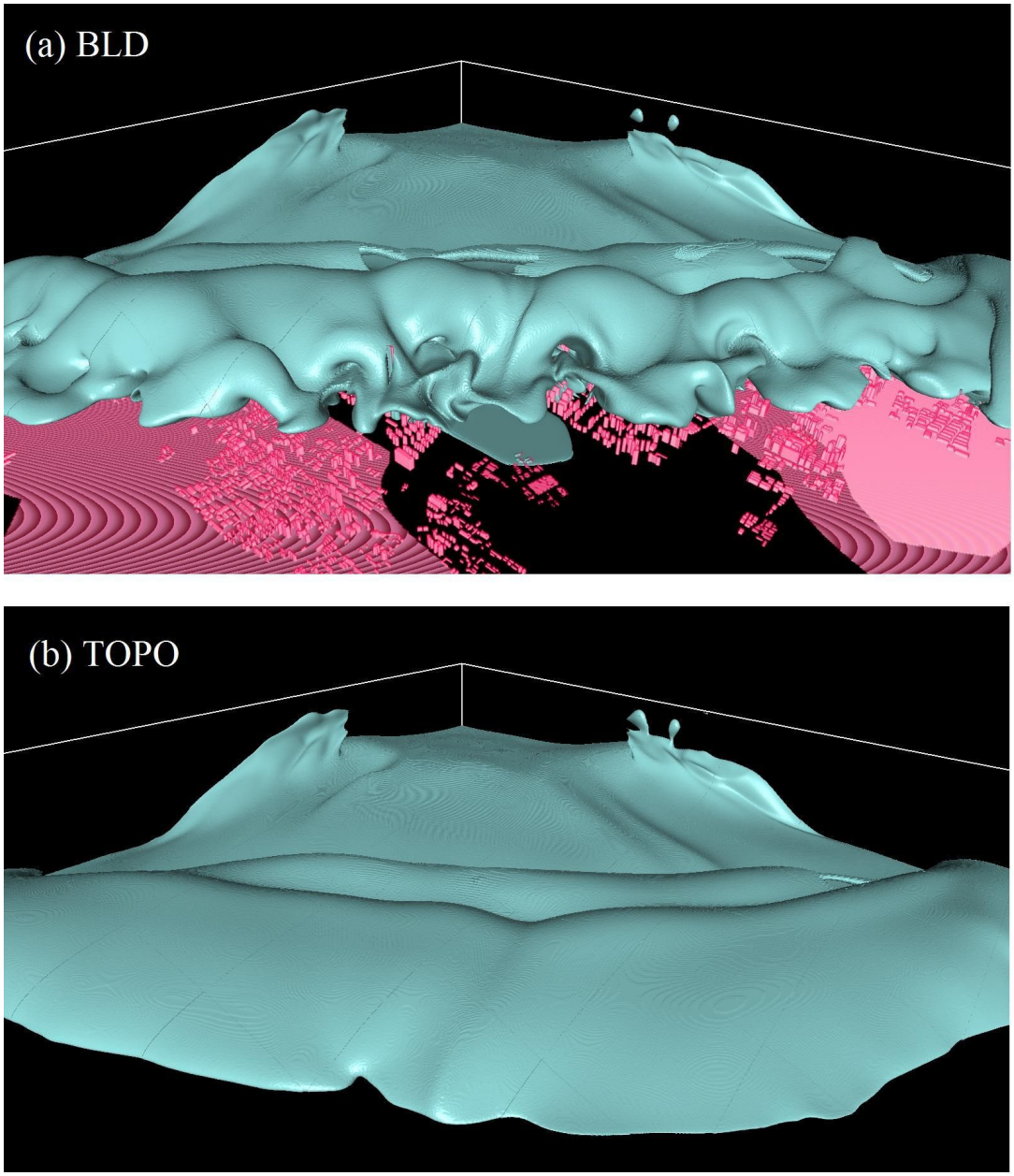

Figure 3.9 Snapshots of 3-dimensional view of front head structures in BLD (a) and TOPO (b) experiments at 580 second. Gray shaded areas indicate isosurfaces of T=295K. Pink blocks in figure 3.9(a) denote building blocks.

3.5 Turbulence statistics

Active turbulence represented by updrafts is generated over urban surface after cold front passes by (Figure 3.10(a)). The turbulence is well organized and displays streaky structures. The organized turbulence structures are developed along the streamwise direction and have a scale much larger than the building size in the elongated direction. Intensified sinking motion appears between two updraft streaks. The locally intensified rising and sinking motion together interrupt cold front and leave a broken front line. In comparison, no obvious turbulence is identified in the TOPO experiment (Figure 3.10(b)). Two lines of rising motion are identified. One is located ahead of cold front, the other one follows. Area between the two rising region is featured by weak vertical motion.

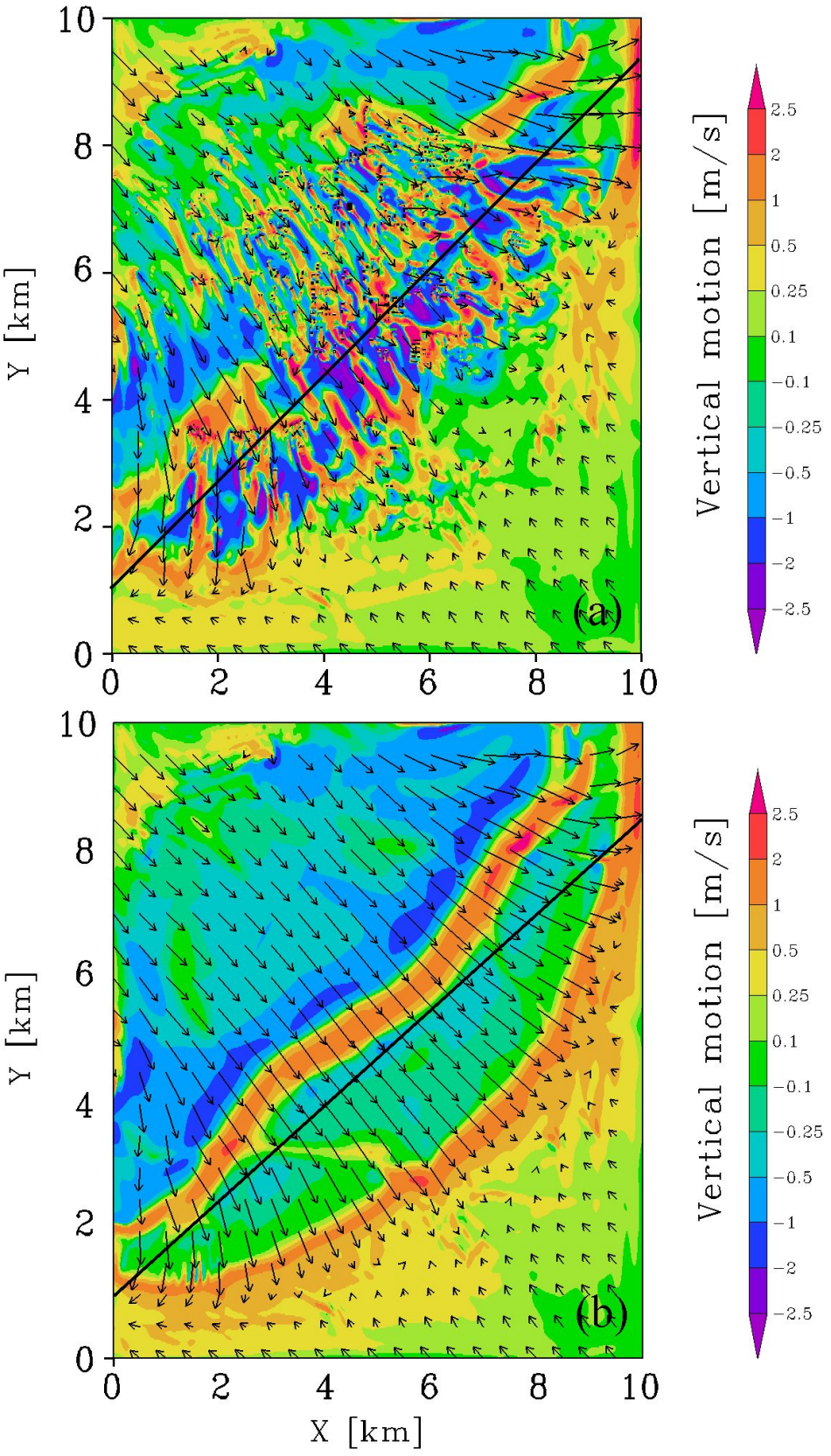

Figure 3.10 Spatial distribution of horizontal wind (vector) and vertical motion (shade) at z=120m at ft=600s in BLD (a) and TOPO (b) experiments. Black lines denote the locations of cross section shown in figure 3.11.

A typical vertical cross section of the front head over buildings is shown in Figure 3.11(a). The distribution of vertical motion clearly indicates that front head is dominate by active turbulence. The rising motion of turbulence structures are generated near surface and extends above buildings. Some of them may even extend to 500 - 600 meters and merge into the front.

In the TOPO experiment, turbulence structures are absent (Figure 3.11(b)). Front head is featured by weak sinking motion.

Figure 3.12 shows the time evolution of vertical velocity spectra. The dramatic increase of energy after front passage (around 300 second) indicates active turbulence generation. The peak of the spectra points out that the turbulence has a scale of 500-600 meters.

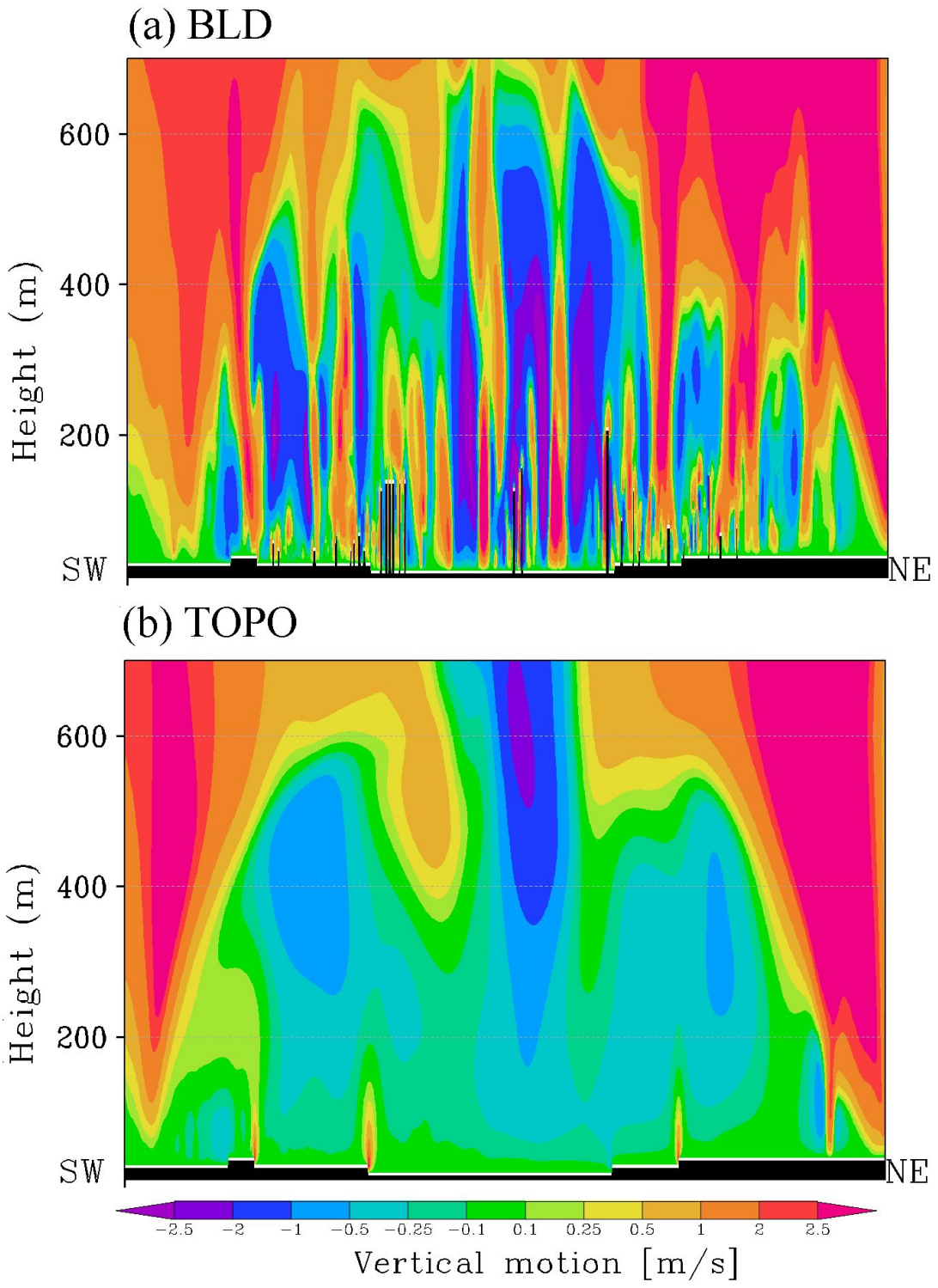

Figure 3.11 Vertical cross section along the front at ft=600s in BLD (a) and TOPO (b) experiments. Locations of the cross section are indicated by lines in figure 3.10.

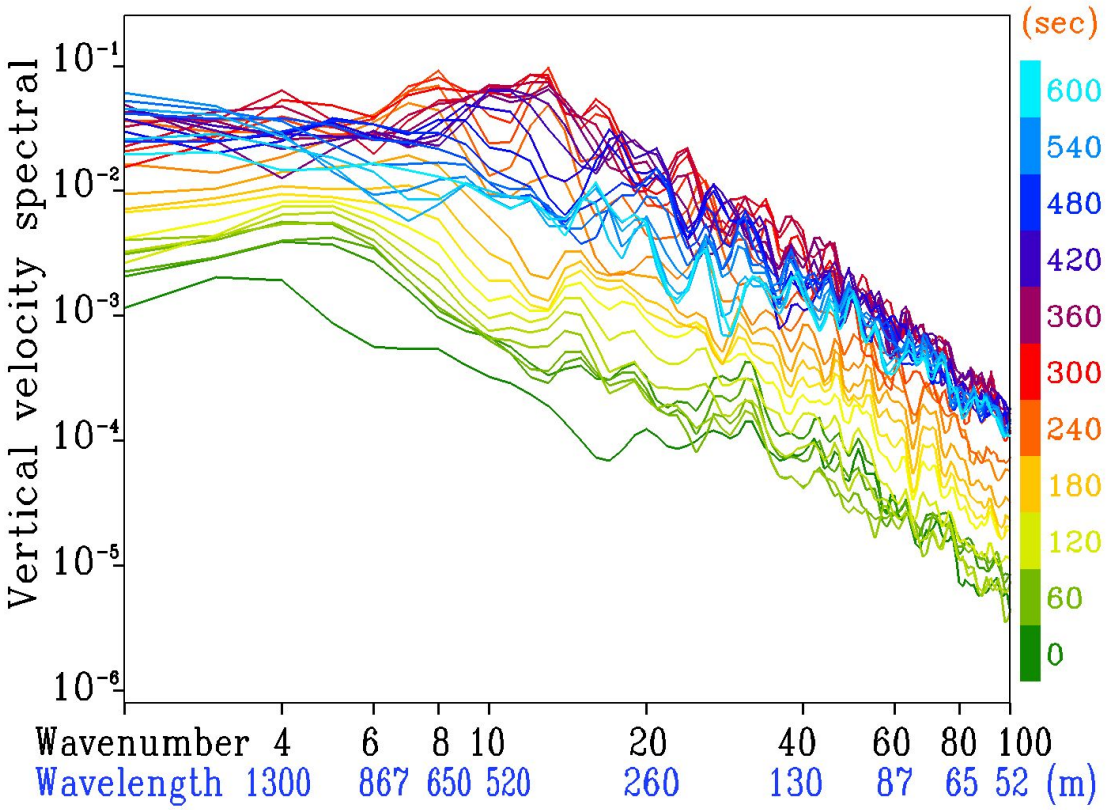

Figure 3.12 Time evolution of vertical velocity spectra at z=160m.

3.6 Impacts of buildings on turbulence organized structures (TOS) generation

3.6.1 TOS generation

The generation of TOS is closely related with urban buildings (Kanda, 2006; Park and Baik, 2014). In order to further clarify the impact of buildings, we take a special look at a typical subdomain in urban area.

Before cold front invades into the subregion, this area is characterized by weak and nondirectional horizontal wind (Figure 3.13(a)). Weak rising motion less than 1 m/s can be identified behind buildings. Temperature displays a horizontally uniform distribution with difference less 0.5 ℃, thus the contours are absent.

After front passes by, strong rising motion of turbulent structures is identified (Figure 3.13(b)). The rising motion is triggered at downwind side of buildings and develops along the streamwise direction. Some updrafts merge together and form one strong streak of rising motion, which can extend more than 500 meters. Temperature at the updrafts can be 1-2 ℃ higher than their surroundings. Sinking motion as strong as 1 m/s is then developed at neighboring areas of the updrafts as a compensation. At the sinking areas, temperature is low and horizontal wind is accelerated significantly compared with the updrafts.

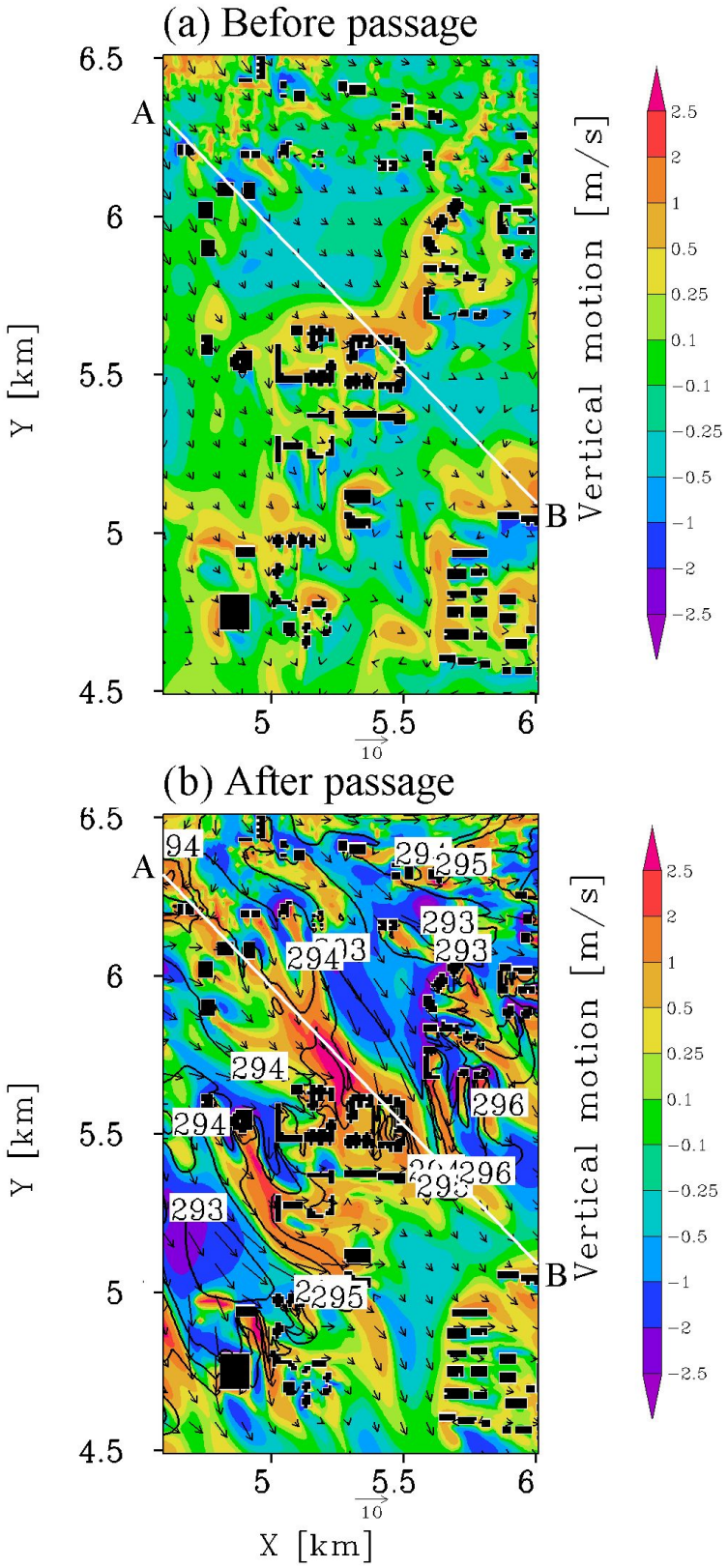

Figure 3.13 Spatial distribution of vertical motion (shade), temperature (contour), and horizontal wind (vector) before (ft=250s) (a) and after (ft=460s) (b) front passage at z=60 m. Black blocks denote buildings. White lines (AB) show the location of cross section in figure 3.14.

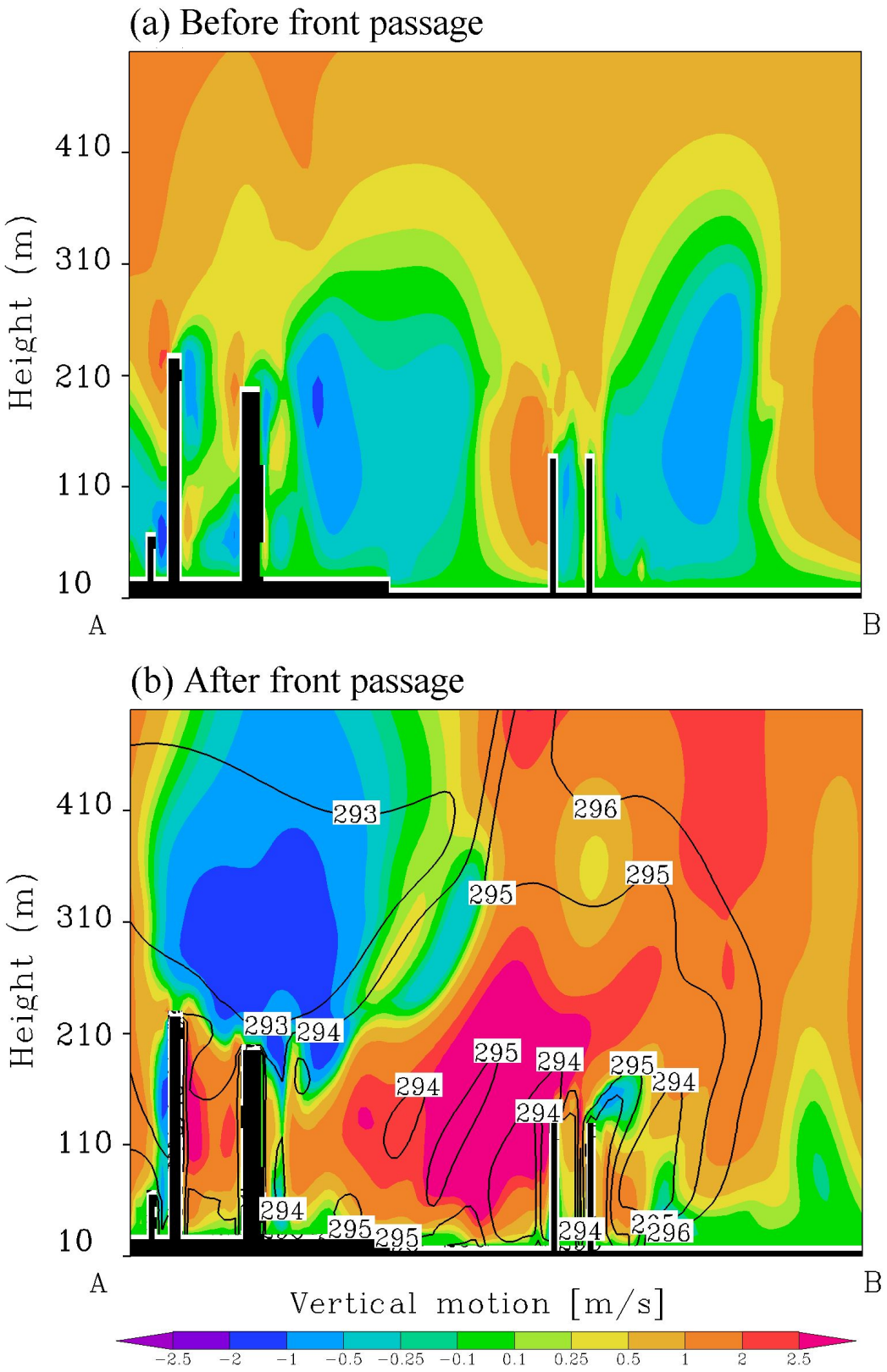

Figure 3.14 Vertical cross section of vertical motion (shade) and temperature (contour) before (ft=300s) (upper) and after (ft=460s) (bottom) front passage. Black blocks denote buildings. Location of the cross section is indicated by the white lines in Figure 3.13.

3.6.2 Turbulent kinetic energy (TKE) budget

The development of building-induced TOS is strongly supported by the TKE. The TKE is very small when front is far away (Figure 3.15). As cold front invades into the subdomain, the TKE begins to increase since around 300 s. Finally, the TKE reaches its maximum when cold front passes through most of the region at around 500 s. The maximum value appears around 70-120 m, a layer above the average building height.

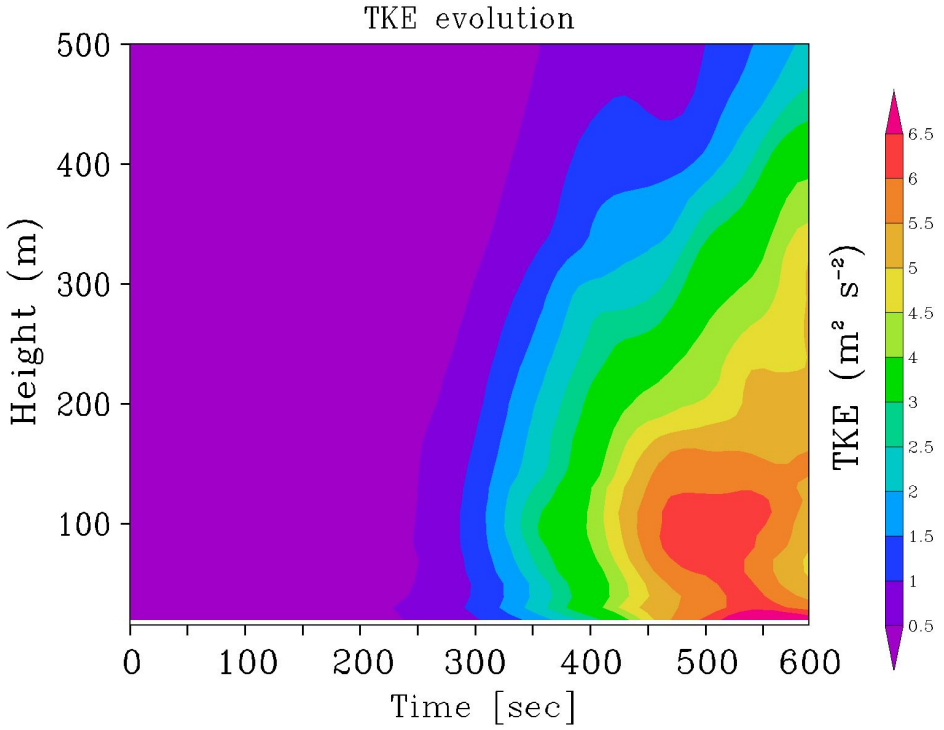

Figure 3.15 Time evolution of the average TKE of the subdomain.

To clarify the processes contributed to the increase of TKE, the TKE budget is investigated. The terms of the TKE budget is given by (Moeng and Sullivan, 1994)

$$\frac{\partial}{\partial t}\overline{E} = -(\overline{u'w'}\frac{\partial \overline{U}}{\partial z} + \overline{v'w'}\frac{\partial \overline{V}}{\partial z}) + \frac{g}{\overline{\theta}}\overline{\theta'w'} - \frac{\partial \overline{w'E'}}{\partial z} - \frac{1}{\rho_0}\frac{\partial \overline{w'p'}}{\partial z} + \varepsilon \qquad (1),$$

where the primes denote perturbations, and the overbars denote spatial means. The first term on the right is the shear production. The second term is the buoyancy production. The third term is the turbulence transport and the fourth is the pressure transport. The last term is the dissipation term.

Before cold front invades into this subdomain, all four terms are small (Figure

3.16(a)). After cold front passes through this region, the four terms increase significantly (Figure 3.16(b)). Shear production grows dramatically below 300 meters, a level within the height of cold front. Its contribution reaches maximum value at around 120 meters above the building roof. Right below this level, fluctuations of horizontal wind (u and v) reach their maximum. Contribution from buoyancy production is large over a wider vertically range than shear production. It reaches maximum value at around 250 meters, with the maximum contribution smaller than that of shear production. At this level, turbulent heat flux also have its maximum value. It is also noted that this level is higher than the level where shear production reaches maximum. Turbulent transport is negative near surface and becomes positive at middle level between 100 meters and 220 meters. It becomes negative again above around 220 meters and decreases to near zero above about 350 meters. Pressure transport is also near zero above about 350 meters. At lower level, it is positive at most time. While it expresses negative values at around 150 meters as well as near surface. It is also noted that pressure transport contributes largely near surface, which helps to form the updrafts.

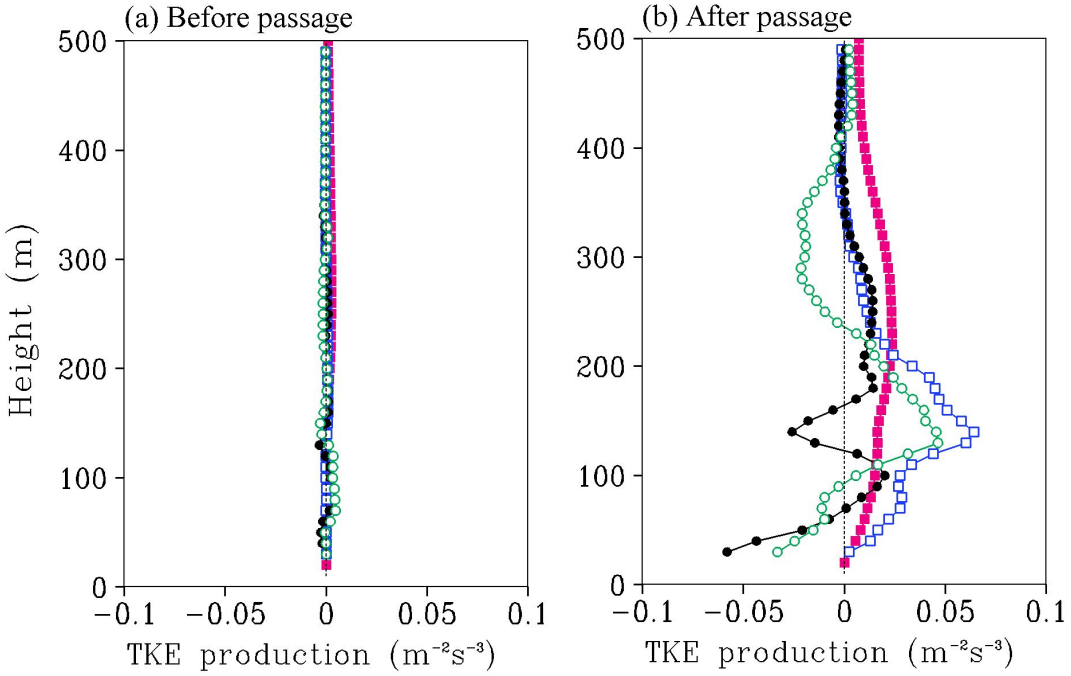

Figure 3.16 Vertical profile of regional averaged TKE production by buoyancy (red), shear (blue), turbulent transport (green), and pressure transport (black) before (a) and after (b) front passage.

3.7 Impacts of TOS on front

3.7.1 Influence on front structure

The building-induced turbulence structures would interact with cold front and result in the deformation of front head structures shown in figure 3.9(a). In order to further investigate the interaction between turbulence structures and front, a composition of the intersections where turbulence merges into front is made (Figure 3.17(a)). Rising motion of the turbulence is triggered behind buildings due to warm air remained after front passage. Then the rising motion is developed and strengthened along the streamwise direction. Finally, it merges with the front and reaches its maximum intensity. Positive temperature perturbation aligns along the updraft and accompanies its intensification. At neighboring areas of the updraft, strong sinking motion is developed. They two together lead to a deformed front head compared with the situation when building-induced turbulence is absent shown in figure 3.17(b). In the TOPO experiment, cold front head displays regular distribution of vertical motion as well as temperature. Smooth contours of temperature indicate a curved front head. Ahead of the front, uniform rising motion at a magnitude between 1-2 m/s is the major feature. After the front, weak sinking motion less than 0.5 m/s is dominate. Both of the vertical motion have a smaller magnitude than that in the BLD composition result. The transition zone from rising motion to sinking motion displays an arc shape and corresponded with the temperature gradients.

Vertical structures along the rising and sinking motion of turbulence are examined. In the cross section A of the rising area, updraft is generated near surface within front head and develops along the downstream side (Figure 3.18(a)). Finally, this building-induced updraft merges with the rising motion ahead of the front. The confluence the two rising motion extend strong rising motion larger than 2 m/s to near surface. At neighboring cross section B, strong sinking motion is formed after front (Figure 3.18(b)). While the strong rising motion (> 2 m/s) ahead of front appears at upper level higher than 400 m. Thermal structures of front head are corresponded with the vertical motion. At the rising area, isosurface is lifted. For example, the isosurface

of 294.5 K locates at around 520 m in the rising area (figure 3.18(a)), while it locates at 490 m in the sinking area (figure 3.18(b)). Such kind of deformation of isosurface by vertical motion results in the 3-dimensional structures of front head in figure 3.9(a).

It is also noted that small-scale eddies are active in front head with the presence of buildings (Figures 3.18(a), (b)). While in the TOPO experiment, front head is characterized by calm conditions without eddies (Figure 3.18(c)). These small-scale eddies generate strong vertical mixing within the front head. As a result, temperature gradient of cold front is decreased as shown by the loose temperature contour both vertically (figures 3.18(a), (b)) and horizontally (figure 3.17 (a)) compared with that in TOPO experiment (figure 3.18(c), figure 3.17 (b)).

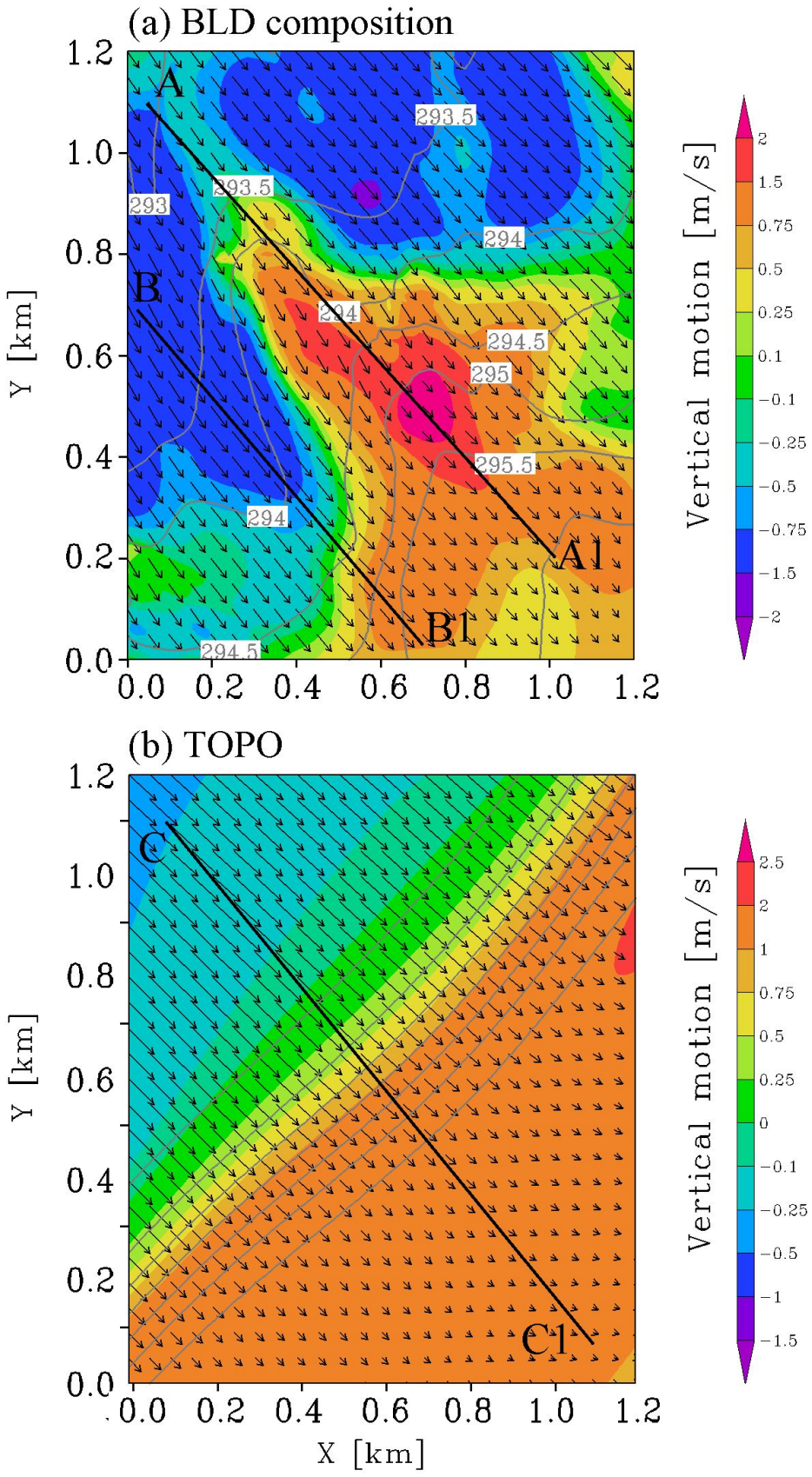

Figure 3.17 Spatial distribution of horizontal wind (vector), vertical motion (shade) and temperature (gray contour) at z=200m in BLD (a) and TOPO (b) experiments. Black lines show the locations of cross section in figure 3.18.

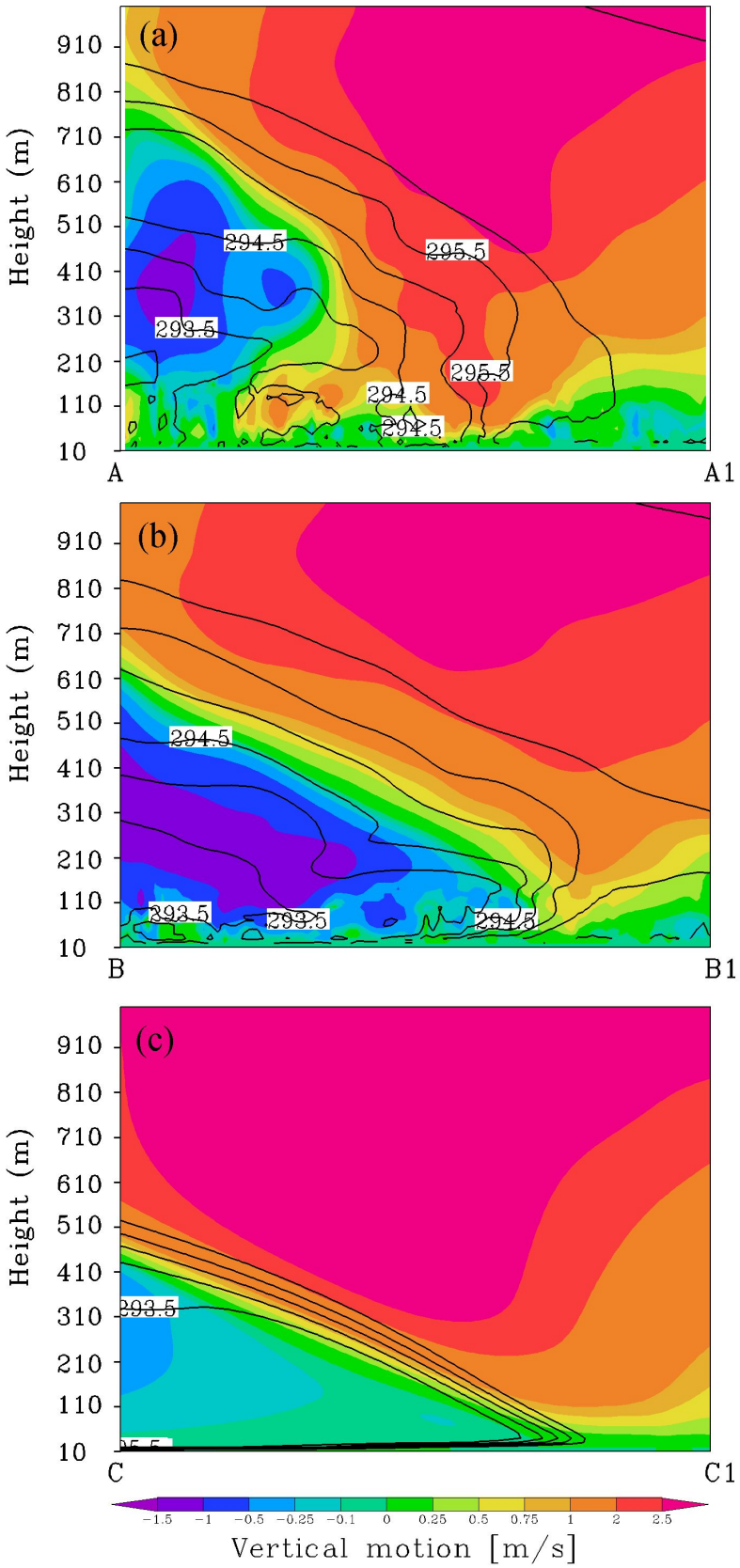

Figure 3.18 Vertical cross section of A, B, C. Shade denotes vertical motion and contour denotes temperature. Locations of cross section A, B, C are indicated by the black lines in figure 3.17.

3.7.2 Influence on transportation process

The regulated cold front over urban surface would then affect the transportation process. Turbulent heat flux distribution in the BLD composition shows a localized pattern related with the vertical motion in Figure 3.17(a) (Figure 3.19(a)). Positive flux appears mainly in four areas. In other areas, flux is near zero. On the other hand, turbulent heat flux in the TOPO experiment displays an even distribution along the front line (Figure 3.19(b)). Strong positive flux appears ahead of front and weak positive flux follows after front.

In order to quantify the separated contributions of different motions to the turbulent heat flux, a quadrant analysis is performed following a typical definition from Raupach (1981). This effective method is often used in turbulence studies (Sullivan et al. 1998; Park and Baik, 2013). Turbulent heat flux is decomposed into four components based on the signs of temperature (t) and vertical velocity (w) fluctuations from the spatial means. The definition is as follows

$$w'\theta' = w'_{+}\theta'_{+} + w'_{+}\theta'_{-} + w'_{-}\theta'_{-} + w'_{-}\theta'_{+} \quad (2)$$

in which the subscripts + and - denote the sign of fluctuation component.

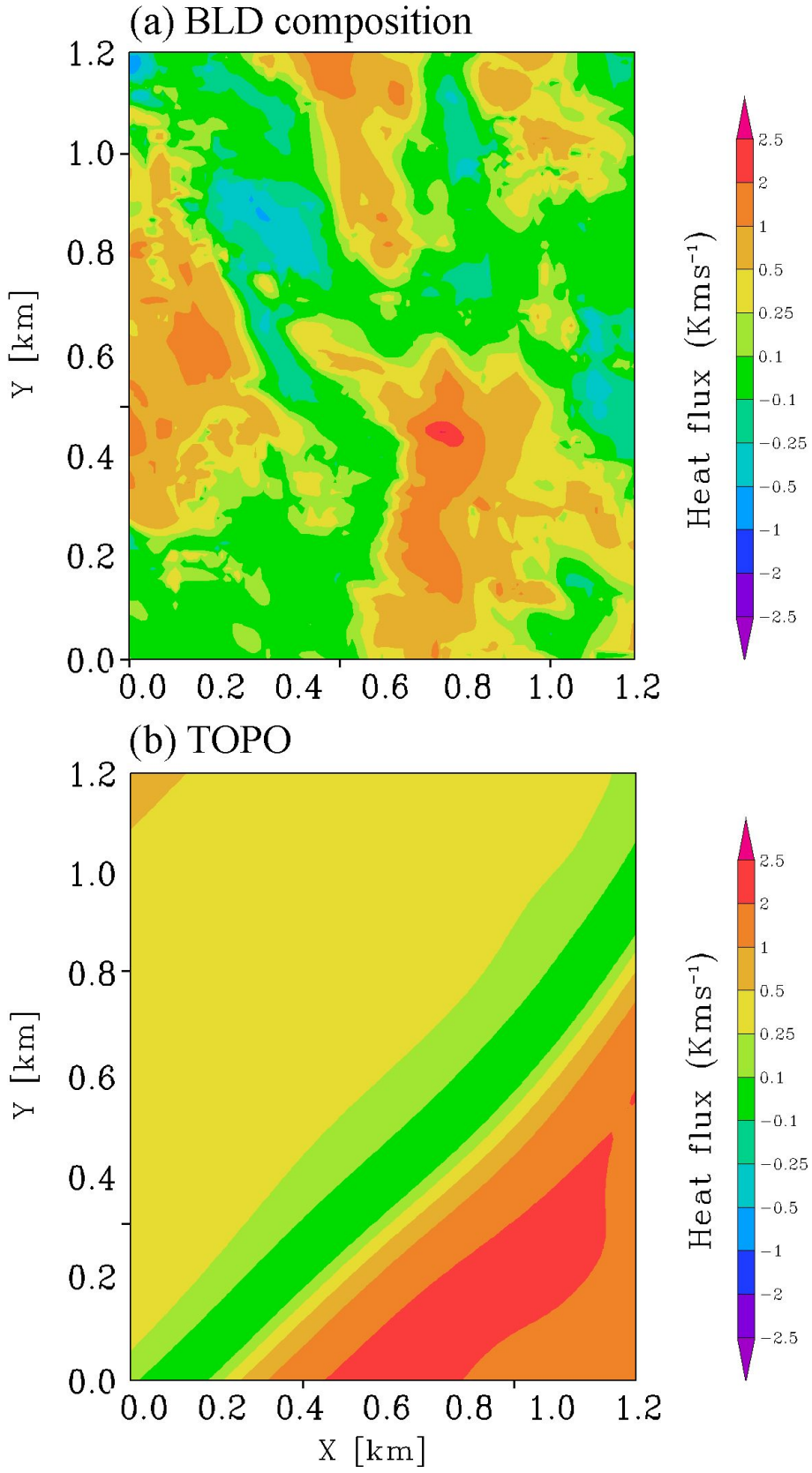

Figure 3.19 Spatial distribution of turbulent heat flux at z=100 m and ft=600s in the BLD experiment composition (a) and TOPO experiment (b).

Ejections (quadrant 1,t+w+) and sweeps (quadrant 3,t-w-) play a significant role in turbulent heat flux transportation (Figure 3.20). Ejections, which are the rising of warming air, contribute positively to the turbulent heat flux at the updraft of turbulence as well as the rising areas ahead of cold front. While sweeps, which are the sinking of cold air, appear at the strong sinking areas neighboring to turbulent updraft after front.

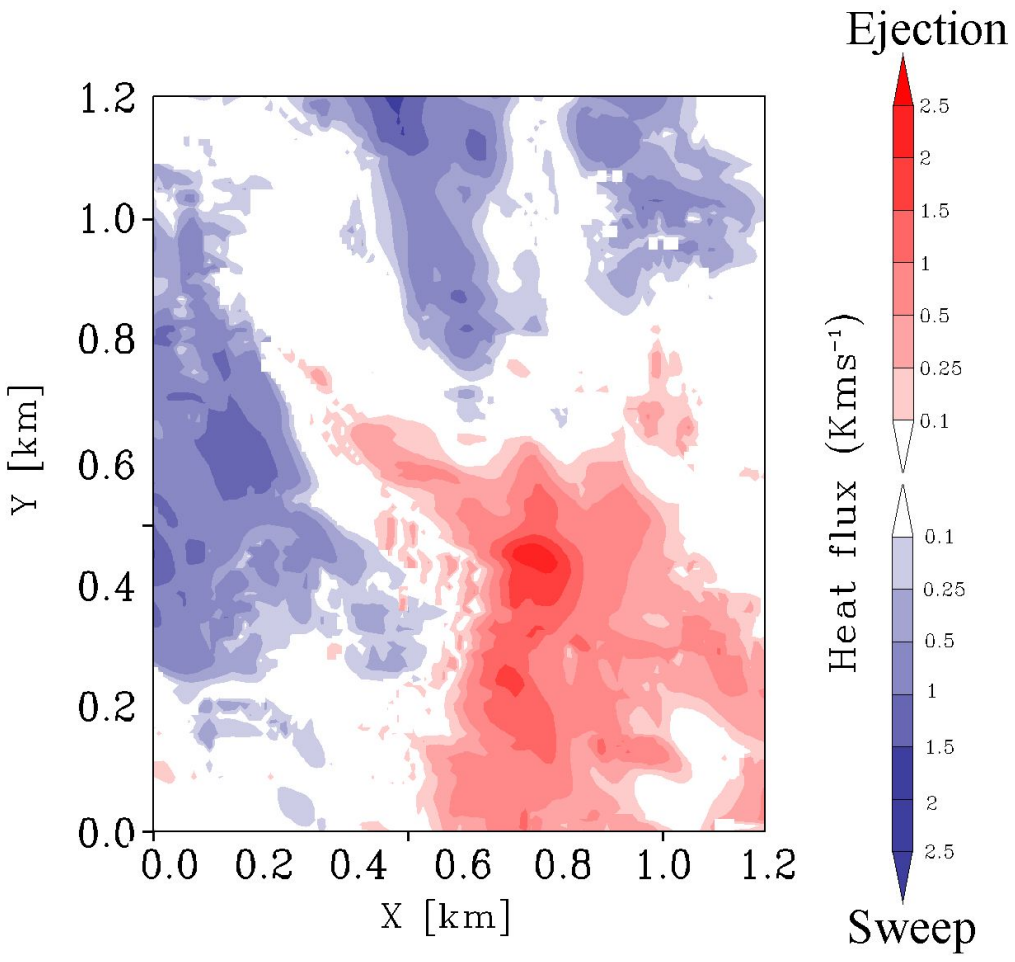

Figure 3.20 Spatial distribution of turbulent heat flux contributed by ejections (red) and sweeps (blue) at z=100 m, ft=600s.

3.8 Strong winds near surface

Urban buildings not only affect cold front structures, but also expresses crucial impact on the surface wind field. Figure 3.21 shows the surface wind field at a small domain when cold front passes through this region from northwest. Strong winds are aligned along the streets due to the tunnel effect of buildings. As a result, cold air mass passes through the street rapidly. On the other hand, wind speed behind buildings is low. Thus warm air mass is easily remained and triggers updrafts.

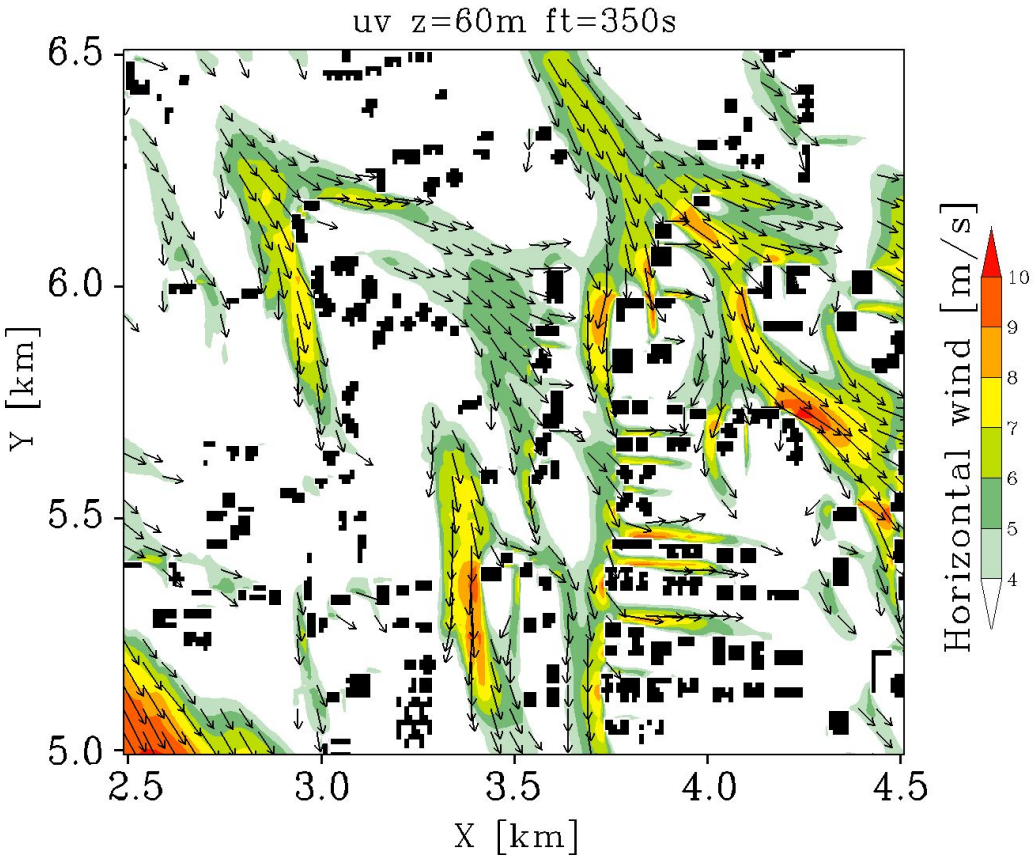

Figure 3.21 Spatial distribution of horizontal wind (>4m/s) at z=60 m and t=350s.

3.9 Summary

In this study, a city-scale simulation of cold front passage at super high resolution is performed. In order to investigate the turbulence structure and its interaction with cold front, two experiments are designed. In this numerical experiment, we pay special attention to the interactions between (building-induced) turbulence structures and cold front.

Modeling results indicate that front structures differ dramatically between with and without buildings. In the presence of buildings, cold front is slowed down and separates into upper and lower parts. Cold front head is regulated and formed 3-d structures due to the interactions with urban surface. Urban buildings induce streaky turbulence structures after front passage. These turbulence structures have a scale of 500-600 meters, which is much larger than building size.

Urban buildings play an important role in triggering turbulence structures. Before front passage, the region is characterized by calm condition with weak and small scale rising motion behind buildings. After front passage, rising motion is induced as a result of the warm air remained behind buildings. The rising motion strengthens and elongates along the streamwise direction, forming the streaky structures. At neighboring areas of rising motion, streaks of sinking motion are developed as an compensation. These streaky structures finally converge with the front. The development of streaky turbulence structures is strongly supported by the turbulent kinetic energy. With increasing contributions from shear and buoyancy production, this energy grows as cold front approaches and passes by. It reaches maximum value after front passage.

The building-induced turbulence structures interact with cold front and regulate front head structures. After front passage, rising motion is triggered behind buildings due to the warm air remained. Developed and strengthened along the streamwise direction, the rising motion finally merges with the upward flow ahead of front. The confluence of the two rising motion extends strong rising motion ahead of front from

middle level to near surface. At neighboring areas of rising motion, strong sinking motion is developed after front. Active small scale eddies within front head decreases the temperature gradient of cold front both horizontally and vertically. As a result, front structures is interrupted and evolved into 3-d structures with bumps and dents through interactions with turbulence structures.

The regulated cold front affects transportation process. Transportation of turbulent heat flux is locally intensified at ejection (rising of warm air) and sweep (sinking of cold air) events.

Urban buildings also express impact on the distribution of wind near surface when front passes through. Strong winds aligned along streets are generated due to tunnel effect of buildings. While wind speed is low behind buildings.

Our high resolution simulation results point out the crucial role of interactions between building-induced turbulence and cold front in modifying front head structures. This interaction highlights the significant impact of buildings in regulating local weather. And our urban-scale experiments also provide good examples for extending urban weather researches from street or block scale to city scale.

Chapter 4 Conclusions and future works

4.1 Conclusions

Thermal effects and mechanical effects, which are the two main aspects of urban impacts on regional climate and local weather, are investigated in the present study. Surface temperature increase, which is closely related with urban thermal effects, is examined over eastern China. By taking the complex aspects (e.g. spatial pattern, growth speed) of urban growth into consideration, a comprehensive evaluation of urbanization effect on local temperature change is performed. Mechanical effects modify wind flow over urban surface significantly. The present study pays special attention to the turbulent structures over urban area and its interaction with a mesoscale cold front.

A new measurement of rapid urban growth is proposed in order to evaluate the influence of urbanization. This new measurement considers complex factors of urbanization such as spatial distribution and growth speed, which is little noticed in traditional investigations. The urban growth intensity is estimated using the size of the area experiencing fast night light increase and its distance to temperature-observation sites. In this respect, both the spatial pattern of fast growth area and its relative distance to observation site is quantitatively assessed. By combining the two variables as area size over distance, a quantitative measurement of the strength of rapid urbanization near the observation site is defined. It also can be viewed as an effective radius of rapid urbanization. A larger value of effective radius stands for a stronger urbanization strength with respect to the temperature-observation site.

By using our new-proposed measurement, the impact of rapid urbanization on surface warming at medium/large cities over eastern China is examined. The statistical results show that the surface warming is occurring to a great degree at sites that have undergone rapid urban growth. Such a relation is more likely to occur in

large and mega cities. The rapidly intensifying urban warming at large and mega cities is therefore contributed by an enhanced temperature trend because of rapid urbanization.

The relation between rapid urbanization and surface warming shows regional variations. The relation is most evident in Central and South China, but it varies considerably in northern China. By further dividing this region into six small domains, we take a special look at northern China. A weak impact of urbanization is found at areas where local features are evident, e.g., coastal zone, grassland. In contrast, rapid urbanization displays a strong influence on surface warming at plain, interior land and so on. The various performance of temperature responses to urbanization effect suggests that the strength of urbanization effect may depend partly on its relative importance to other climate forcings such as topography, land-sea contrast, and desertification.

To investigate how surface warming at sites is affected by rapid urbanization, distribution of urban heat island over Pearl River Delta is examined by using remote sensing data. Analysis of satellite-derived land surface temperature suggests that rapid urbanization is generally accompanied by an expansion of urban heat island. The sites affected by urbanization-induced urban heat island expansion tend to experience strong warming. In contrast, for sites far away from rapid urbanization region, they are less affected by the urban heat island expansion and thus report weak warming.

The strong association between temperature trend and rapid urbanization at both regional and local scales is supportive to attributing increased temperature anomaly to rapid urban growth. These results also point to the fact that the urban climate change over eastern China might include an important component of surface warming induced by rapid urbanization.

In chapter 3, we explore the turbulent structures over urban areas through numerical simulations. Different from previous investigations at street scale, our modelings employ a large domain at a whole city scale with building-resolving

resolution. Taking advantage of the urban-scale simulation, we specially focus on the interaction between urban-induced turbulence and a mesoscale cold front. This kind of interaction is little noticed by previously studies.

By comparing the results from with-building and without-building experiments, it is found that active organized turbulent structures are generated over urban surface after a cold front passed through. The turbulent structures as indicated by streaks of vertical motion align along the streamwise direction and have a scale of 500-600 meters, which is much larger than building size. With the streaky turbulent structures, cold front is regulated dramatically by urban surface and form 3-dimensional structures in the with-building experiment. Moreover, cold front is slowed down and separates into upper and lower parts in the presence of buildings.

The generation of turbulent structures over urban surface is closely related with the presence of buildings. When cold front is far, calm winds with weak and small-scale rising motion behind the buildings are the major feature. After cold front passed through, strong and large-scale updrafts are generated. The rising motion is first induced behind buildings as a result of the warm air remained after cold front passage. Then it develops and intensifies along the streamwise direction. Finally, streaky structures of rising motion are formed. At neighboring areas, streaks of sinking motion are developed as an compensation. Both rising motion and sinking motion converge with cold front and modify the front structures.

The development of streaky turbulence structures is strongly supported by the turbulent kinetic energy (TKE). The TKE is very small before cold front passage. The energy grows as cold front approaches and reaches maximum value after front passage. By analyzing the TKE budget, contributions from different forcings are examined.

The building-induced turbulence structures interact with cold front and regulate front head structures. A composition of the areas where turbulent structures meet cold front head clearly indicates their interaction. Due to the warm air remained behind

buildings, rising motion is triggered after cold front passed by. Then it develops and intensifies along the streamwise direction, finally merges with the upward flow ahead of front. The confluence of the updrafts extends strong rising motion ahead of front from middle level to near surface. At neighboring areas of rising motion, strong sinking motion is generated. These downdrafts strengthen sinking motion after front. It is also noted that small-scale eddies are active within cold front head. These small-scale eddies decreases the temperature gradient of cold front both horizontally and vertically. The updrafts and downdrafts of turbulent structures break the cold front and deform it into 3-dimensional structures with bumps and dents.

Our high resolution simulation results identify the strong interaction between turbulent structures and cold front. This interaction regulate front head structures and the transportation process. This result underscores the possible impacts of urban buildings on local weather.

In the actual situation, urban thermal effects and mechanical effects do not work separately. They together show comprehensive influence on urban weather and environments. Our study, which discusses urban impacts on surface warming and turbulent structures, provides new views and implications for urban climate and weather research.

4.2 Future works

Based on the above results, some potential works are available in the future.

In this study, we pointed out the crucial role of rapid urban growth in intensifying surface temperature increase over eastern China. As urbanization expands throughout the world, similar effect of rapid urbanization on urban warming over other countries and regions is expected. We must be cautious about the region-dependent forcings from climate background and local features when perform similar investigation in other regions.

In this study, we focus on the impact of urbanization on surface temperature. Urban growth also expresses significant influence on other meteorological variables, such as wind, moisture, and rainfall (Collier 2006; Li et al. 2011). Examinations of impact of rapid urbanization on these variables are also necessary.

The numerical experiments indicated the possibility of the significant impacts of urban buildings on local weather. Validations from high-resolution observation are necessary.

In our modeling results, strong interaction between building-induced turbulence and cold front is identified. Such kind of interaction is also expected when other mesoscale weather systems pass through urban areas. It is also expected that different mesoscale systems may perform variously when they meet turbulence.

Another application of our down-scaling simulation system is forecasting of extreme weather and disasters. Such kind of prediction has important social implications.

References

Argueso, D., J. Evans, L. Fita, and K. Bormann, 2014: Temperature response to future urbanization and climate change. *Climate Dynamics*, 42 (7), 2183–2199.

Baik, J., and S. Park, 2009: Urban flow and dispersion simulation using a CFD model coupled to a mesoscale model. *Journal of Applied Meteorology and Climatology*, 48, 1667-1681.

Bowne, N., and J. Ball, 1970: Observational comparison of rural and urban boundary layer turbulence. *Journal of Applied Meteorology*, 9, 862-873.

Chao, L., and J. Sun, 2009: Temporal change in annual air temperature and heat island effect in a coastal city and an inland city at mid-latitude in China during 1956-1998. *Chinese Journal of Applied Ecology* (in Chinese), 20 (12), 2839–2846.

Chen, G., X. Zhu, W. Sha, T. Iwasaki, H. Seko, K. Saito, H. Iwai, and S. Ishii, 2015a: Toward improved forecasts of sea-breeze horizontal convective rolls at super high resolutions. Part Ⅰ: Configuration and verification of a down-scaling simulation system (DS^3). *Monthly Weather Review* (in press).

Chen, G., X. Zhu, W. Sha, T. Iwasaki, H. Seko, K. Saito, H. Iwai, and S. Ishii, 2015b: Toward improved forecasts of sea-breeze horizontal convective rolls at super high resolutions. Part Ⅱ: The impacts of land use and buildings. *Monthly Weather Review* (in press).

Christen, A., and R. Vogt, 2004: Energy and radiation balance of a central European city. *International Journal of Climatology*, 24, 1395-1421.

Collier, C. G., 2006: The impact of urban areas on weather. *Quarterly Journal of the Royal Meteorological Society*, 132, 1–25.

Elvidge, C., D. Ziskin, K. Baugh, B. Tuttle, T. Ghosh, D. Pack, E. Erwin, and M. Zhizhin, 2009: A fifteen year record of global natural gas flaring derived from satellite data. *Energies*, 2, 595-622.

Foster, R., F. Vianey, P. Drobinski, and P. Carlotti, 2006: Near-surface coherent structures and the vertical momentum flux in a large-eddy simulation of the neutrally-stratified boundary layer. *Boundary Layer Meteorology*, 120, 229-255.

Fujibe, F., 2009: Detection of urban warming in recent temperature trends in Japan. *International Journal of Climatology*, 29, 1811-1822.

Fujibe, F., 2011: Review: Urban warming in Japanese cities and its relation with climate change monitoring. *International Journal of Climatology*, 31, 162-173.

Guo, X., D. Fu, and J. Wang, 2006: Mesoscale convective precipitation system modified by urbanization in Beijing city. *Atmospheric Research*, 82, 112-126.

Hale, R., K. Gallo, D. Tarpley, and Y. Yu, 2011: Characterization of variability at in situ locations for calibration/validation of satellite-derived land surface temperature data. *Remote Sensing Letters*, 2 (1), 41–50.

He, C., P. Shi, J. Li, J. Chen, Y. Pan, J. Li, L. Zhuo, and T. Ichinose, 2006: Restoring urbanization process in China in the 1990s by using non-radiance-calibrated DMSP/OLS nighttime light imagery and statistical data. *Chinese Science Bulletin*, 51 (13), 1614–1620.

Ichinose, T., K. Shimodozono, and K. Hanaki, 1999: Impact of anthropogenic heat on urban climate in Tokyo. *Atmospheric Environment*, 33, 3897-3909.

Inagaki, A., M. Castillo, Y. Yamashita, M. Kanda, and H. Takimoto, 2011: Large-eddy simulation of coherent flow structures within a cubical canopy. *Boundary Layer Meteorology*, 142, 207-222.

Jin, M., R. E. Dickson, and D. Zhang, 2005: The footprint of urban areas on global climate as characterized by MODIS. *Journal of Climate*, 18, 1551–1565.

Kalnay, E., and M. Cai, 2003: Impact of urbanization and land use change on climate. *Nature*, 423, 528–531.

Kanda, M., R. Moriwaki, and F. Kasamatsu, 2004: Large-eddy simulation of turbulent

organized structures within and above explicitly resolved cube arrays. *Boundary Layer Meteorology*, 112, 343-368.

Kanda, M., 2006: Large-eddy simulation of the effects of surface geometry of building arrays on turbulent organized structures. *Boundary Layer Meteorology*, 118, 151-168.

Karl, T., H. Diaz, and G. Kukla, 1988: Urbanization: its detection and effect in the United States climate record. *Journal of Climate,* 1, 1099–1123.

Khanna, S., and J. Brasseur, 1998: Three-dimensional buoyancy- and shear- induced local structures of the atmospheric boundary layer. *Journal of the Atmospheric Sciences*, 55, 710-743.

Li, Q., H. Zhang, X. Liu, and J. Huang, 2004: Urban heat island effect on annual mean temperature during the last 50 years in China. *Theoretical and Applied Climatology*, 79, 165–174.

Li, Q., W. Li, P. Si, X. Gao, W. Dong, P. Jones, J. Huang, and L. Cao, 2010: Assessment of surface air warming in northeast China, with emphasis on the impacts of urbanization. *Theoretical and Applied Climatology*, 99, 469–478.

Li, W., S. Chen, G. Chen, W. Sha, C. Luo, Y. Feng, Z. Wen, and B. Wang, 2011: Urbanization signatures in strong versus weak precipitation over the Pearl River Delta metropolitan regions of China. *Environmental Research Letters*, 6, 034020.

Lin, W., C. Sui, L. Yang, X. Wang, R. Deng, S. Fan, C. Wu, A. Wang, S. Fong, and H. Lin, 2007: A numerical study of the influence of urban expansion on monthly climate in dry autumn over the Pearl River Delta, China. *Theoretical and Applied Climatology*, 89, 63–72.

Liu, H., and J. Chan, 2001: An investigation of air-pollutant patterns under sea breezes during a severe air-pollution episode in Hong Kong. *Atmospheric Environment*, 36, 591-601.

Ma, L., T. Zhang, Q. Li, O. Franenfeld, and D. Qin, 2008: Evaluation of ERA-40,

NCEP-1, and NCEP-2 reanalysis air temperatures with ground-based measurements in China. *Journal of Geophysical Research*, 113, D12115.

Ma, T., C. Zhou, T. Pei, S. Haynie, and J. Fan, 2012: Quantitative estimation of urbanization dynamics using time series of DMSP/OLS nighttime light data: A comparative case study from China's cities. *Remote Sensing of Environment*, 124, 99–107.

Martilli, A., 2002: Numerical study of urban impact on boundary layer structure: sensitivity to wind speed, urban morphology, and rural soil moisture. *Journal of Applied Meteorology*, 41, 1247-1266.

Melas, D., I. Ziomas, and C. Zerefos, 1995: Boundary layer dynamics in an urban coastal environment under sea breeze conditions. *Atmospheric Environment*, 29, 3605-3617.

Moeng, C., and P. Sullivan, 1994: A comparison of shear- and buoyancy-driven planetary boundary layer flows. *Journal of the Atmospheric Sciences*, 51 (7), 999-1022.

Oikawa, S., and Y. Meng, 1995: Turbulence characteristics and organized motion in a suburban roughness sublayer. *Boundary Layer Meteorology*, 74,289-312.

Oke, T. R., 1973: City size and the urban heat island. *Atmospheric Environment*, 7, 769–779.

Oke, T. R, 1988: The urban energy balance. *Progress in Physical Geography*, 12, 471–508.

Park, S., and J. Baik, 2013: A large-eddy simulation study of thermal effects on turbulent coherent structures in and above a building array. *Journal of applied meteorology and climatology*, 52, 1348-1365.

Park, S., and J. Baik, 2014: Large-eddy simulations of convective boundary layers over flat and urbanlike surfaces. *Journal of the Atmospheric Sciences*, 71, 1880-1892.

Qiao, Z., G. Tian, and L. Xiao, 2013: Diurnal and seasonal impacts of urbanization on the urban thermal environment: A case study of Beijing using MODIS data. *ISPRS Journal of Photogrammetry and Remote Sensing,* 85, 93–101.

Raupach, M., 1981: Conditional statistics of Reynolds stress in rough-wall and smooth-wall turbulent boundary layers. *Journal of Fluid Mechanics*, 108, 363-382.

Ren, G., Y. Ding, Z. Zhao, J. Zheng, T. Wu, G. Tang, and Y. Xu, 2012: Recent progress in studies of climate change in North China. *Advances in Atmospheric Science*, 29 (5), 958–977.

Ren, G., Y. Zhou, Z. Chu, J. Zhou, A. Zhang, J. Guo, and X. Liu, 2008: Urbanization effects on observed surface air temperature trends in north China. *Journal of Climate*, 21, 1333–1348.

Rizwan, A., L. Dennis, and C. Liu, 2008: A review on the generation, determination and mitigation of Urban Heat Island. *Journal of Environmental Sciences,* 20, 120–128.

Roth, M., 2000: Review of atmospheric turbulence over cities. *Quarterly Journal of the Royal Meteorological Society*, 126, 941-990.

Roth, M., and T. Oke, 1993: Turbulent transfer relationships over an urban surface. Ⅰ: Spectral characteristics. *Quarterly Journal of the Royal Meteorological Society*, 119, 1071-1104.

Rozoff, C., W. Cotton, and J. Adegoke, 2002: Simulation of St.Louis, Missouri, land use impacts on thunderstorms. *Journal of Applied Meteorology*, 42, 716-738.

Saito, K., and Coauthors, 2006: The operational JMA nonhydrostatic mesoscale model. *Month Weather Review*, 134, 1266‐1298.

Saito, K., J. Ishida, K. Aranami, T. Hara, T. Segawa, M. Narita, and Y. Honda, 2007: Nonhydrostatic atmospheric models and operational development at JMA. *Journal of Meteorological Society of Japan*, 85B, 271‐304.

Schols, J., 1984: The detection and measurement of turbulent structures in the atmospheric surface layer. *Boundary Layer Meteorology*, 24, 39-58.

Sha, W., T. Kawamura, and H. Ueda, 1991: A numerical study on sea/land breezes as a gravity current: Kelvin‐Helmholtz billows and inland penetration of the sea-breeze front. *Journal of the Atmospheric Sciences*, 48, 1649‐1665.

Sha, W., 2002: Design of the dynamics core for a new-generation numerical model of the local meteorology. *Kaiyo Monthly* (in Japanese), 2, 107‐112.

Sha, W., 2008: Local meteorological model based on LES over the Cartesian coordinate and complex surface. *Meteorological Research Note* (in Japanese), edited by Y. Fujiyoshi, 219, pp. 21 ― 26, Meteorological Society of Japan press, Tokyo, Japan.

Sullivan, P., C. Moeng, B. Stevens, D. Lenschow, and S. Mayor, 1998: Structures of the entrainment zone capping the convective atmospheric boundary layer. *Journal of the Atmospheric Sciences*, 55, 3042-3064.

Sutton, P., D. Roberts, C. D. Elvidge, and K. Baugh, 2001: Census from heaven: An estimate of the global human population using night-time satellite imagery. *International Journal of Remote Sensing,* 22 (16), 3061–3076.

Taha, H., 1997: Urban climates and heat islands: albedo, evapotranspiration and anthropogenic heat. *Energy and Buildings*, 25, 99–103.

Thielen, J., W. Wobrock, A. Gadian, P. Mestayer, and J. Creutin, 2000: The possible influence of urban surfaces on rainfall development: a sensitivity study in 2D in the meso-r-scale. *Atmospheric Research*, 54, 15-39.

Tomlinson, C., L. Chapman, J. Thornes, C. Baker, and T. Lopez, 2012: Comparing night-time satellite land surface temperature from MODIS and ground measured air temperature across a conurbation. *Remote Sensing Letters*, 3 (8), 657–666.

Tsutsumi, J., T. Katayama, T. Hayashi, and H. Kitayama, 1990/91: Statistical analysis for the characteristics of sea-land breeze and its effect on urban thermal

environment. *Energy and Buildings*, 15-16, 1003-1008.

Wan, Z., Y. Zhang, Q. Zhang, and Z. Li, 2004: Quality assessment and validation of the MODIS global land surface temperature. *International Journal of Remote Sensing,* 25 (1), 261–274.

Wang, T., W. Wu, X. Xue, Q. Sun, W. Zhang, and Z. Han, 2004: Spatial-temporal changes of sandy desertified land during last 5 decades in Northern China. *Acta Geographica Sinica* (in Chinese)*,* 59 (2), 203–212.

Wang, X., P. Xiao, X. Feng, and H. Li, 2013: Extraction of large-scale urban area information in China using DMSP/OLS nighttime light data. *Remote Sensing for Land and Resources* (in Chinese), 25 (3), 159–164.

Welch, R., 1980: Monitoring urban population and energy utilization patterns from satellite data. *Remote Sensing of Environment*, 9, 1–9.

Xue, Y., 1996: The impact of desertification in the Mongolian and the inner Mongolian grassland on the regional climate. *Journal of Climate*, 9, 2173–2189.

Yang, X., Y. Zhang, L. Liu, W. Zhang, M. Ding, and Z. Wang, 2009: Sensitivity of surface air temperature change to land use/cover types in China. *Science China Series D-Earth Science,* 52 (8), 1207–1215.

Yang, X., Y. Hou, and B. Chen, 2011: Observed surface warming induced by urbanization in east China. *Journal of Geophysical Research,* 116, D14113.

Zhong, S., and X. Yang, 2015: Ensemble simulations of the urban effect on a summer rainfall event in the Great Beijing Metropolitan Area. *Atmospheric Research*, 153, 318-334.

Zhou, L., R. Dickinson, Y. Tian, J. Fang, Q. Li, R. Kaufmann, C. Tucher, and R. Myneni, 2004: Evidence for a significant urbanization effect on climate in China. *Proceedings of the National Academy of Sciences, USA*, 101 (26), 9540–9544.

Acknowledgments

I would like to express my deep indebtedness to the professors for their support and advices. In particular, I would like to appreciate my supervisor Prof. Sha Weiming for his patient guidance and ceaseless support. And I also would like to thank Prof. Toshiki Iwasaki and Prof. Takeshi Yamazaki for their useful advice and valuable support on my study.

More over, I am also grateful for all members of the Atmospheric Science Laboratory, especially Dr. Chen Guixing for his valuable suggestion and assistance since the beginning of my research, the PC staff students for computer maintenance, Ms. Saeko Hasebe for the help and support in all my study administrations, and other members for their advice and information.

Further, I also would like to express my thanks to the Ministry of Education, Culture, Sports, Science and Technology (Mombukagakusho) Japan who has financially supported my study in Japan. Moreover, I would like to thank the Future Global Leadership Program and the Takuetsu Program for providing the job of research assistant and covering my travel expenses for oversea meetings. Thanks also goes to the IGPAS project of Graduate School of Tohoku University, which has offered such a wonderful opportunity to carry out my research in Japan.

I also would like to express my thanks to the Cyberscience Center, Tohoku University for using the supercomputer to carry out my high-resolution simulations as well as the Japan Meteorological Agency and Meteorological Research Institute for using their Non-Hydrostatic Model (JMA-NHM).

Finally, I appreciate all, who are not mentioned here, for their help, either direct or indirect, so that I can finish my study.